



Over a 10-year record of aerosol optical properties at SMEAR II

Krista Luoma¹, Aki Virkkula^{1,2}, Pasi Aalto¹, Tuukka Petäjä¹, and Markku Kulmala¹

¹Institute for Atmospheric and Earth System Research, University of Helsinki, Helsinki, 00014, Finland

²Atmospheric Composition Research, Finnish Meteorological Institute, Helsinki, 00560, Finland

Correspondence: Krista Luoma (krista.q.luoma@helsinki.fi) and Aki Virkkula (aki.virkkula@fmi.fi)

Received: 14 September 2018 – Discussion started: 12 November 2018

Revised: 27 July 2019 – Accepted: 29 July 2019 – Published: 9 September 2019

Abstract. Aerosol optical properties (AOPs) describe the ability of aerosols to scatter and absorb radiation at different wavelengths. Since aerosol particles interact with the sun's radiation, they impact the climate. Our study focuses on the long-term trends and seasonal variations of different AOPs measured at a rural boreal forest site in northern Europe. To explain the observed variations in the AOPs, we also analyzed changes in the aerosol size distribution. AOPs of particles smaller than $10\text{ }\mu\text{m}$ (PM_{10}) and $1\text{ }\mu\text{m}$ (PM_1) have been measured at SMEAR II, in southern Finland, since 2006 and 2010, respectively. For PM_{10} particles, the median values of the scattering and absorption coefficients, single-scattering albedo, and backscatter fraction at $\lambda = 550\text{ nm}$ were 9.8 Mm^{-1} , 1.3 Mm^{-1} , 0.88, and 0.14. The median values of scattering and absorption Ångström exponents at the wavelength ranges 450–700 and 370–950 nm were 1.88 and 0.99, respectively. We found statistically significant trends for the PM_{10} scattering and absorption coefficients, single-scattering albedo, and backscatter fraction, and the slopes of these trends were -0.32 Mm^{-1} , -0.086 Mm^{-1} , 2.2×10^{-3} , and 1.3×10^{-3} per year. The tendency for the extensive AOPs to decrease correlated well with the decrease in aerosol number and volume concentrations. The tendency for the backscattering fraction and single-scattering albedo to increase indicates that the aerosol size distribution consists of fewer larger particles and that aerosols absorb less light than at the beginning of the measurements. The trends of the single-scattering albedo and backscattering fraction influenced the aerosol radiative forcing efficiency, indicating that the aerosol particles are scattering the radiation more effectively back into space.

1 Introduction

Aerosols affect the radiative balance of the atmosphere both directly by aerosol–radiation interactions (ARIs), i.e., by scattering and absorbing solar radiation and by absorbing and emitting terrestrial infrared radiation, and indirectly by aerosol–cloud interactions (ACIs), i.e., by influencing the properties and processes of clouds (Charlson et al., 1992; Lohmann and Feichter, 2005; Ramanathan et al., 2001; Stocker et al., 2013). The uncertainty of the estimated radiative forcing of climate by ACI is larger than that by ARI but the latter is also substantial (Stocker et al., 2013). Both ARI and ACI have been shown to be responsible for dimming, the reduction of solar radiation received at the surface of the Earth (Wild, 2009, 2012; Stocker et al., 2013). Dimming and brightening have been shown to be often reconcilable with the trends in anthropogenic emissions of aerosols and their precursors and atmospheric aerosol loadings (Wild, 2012).

Aerosol optical properties (AOPs) describe the ability of aerosol particles to absorb and scatter radiation at different wavelengths. Knowing how aerosol particles interact with radiation is essential in determining the direct effect that aerosols have on the climate. The direct effect of aerosol can be either warming or cooling, depending on the AOPs and the properties of the surface below the aerosol layer (Haywood and Shine, 1995). Determining the global radiative forcing (RF) related to the direct effect of aerosol particles has vast uncertainties (Stocker et al., 2013), which are due to the wide spatial and temporal variations in the number concentration, chemical composition, and size distribution of aerosol particles, so it is challenging to consider them in climate models.

Making long-term observations of aerosol concentrations and properties at several regionally representative sites is necessary to understand and quantify the global influence of

aerosols (e.g., Laj et al., 2009; WMO/GAW, 2012; Weatherhead et al., 2018; Andrews et al., 2019). There are several networks of stations where such measurements are conducted, both global and regional (Pandolfi et al., 2018; WMO/GAW, 2012). The goal of the Global Atmosphere Watch (GAW) is to ensure long-term measurements of atmospheric variables in order to detect trends and reasons for those trends (WMO/GAW, 2012). This can be considered the goal of all long-term aerosol measurements. Trends in AOPs can also be used as indicators of emission control measures (Pandolfi et al., 2018). Recently Collaud Coen et al. (2013) presented trends of in situ AOPs at 24 GAW and IMPROVE stations, Sherman et al. (2015) presented trends of AOPs at four North American surface monitoring sites, Lihavainen et al. (2015) presented trends of AOPs at the Pallas GAW station, and Pandolfi et al. (2018) presented trends of scattering coefficients at 28 ACTRIS observatories located mainly in Europe.

Here we present the results of long-term measurements of AOPs at SMEAR II (Station for Measuring Ecosystem–Atmosphere Relations; Hari and Kulmala, 2005). The location represents the typical conditions of a boreal forest (Hari et al., 2013), which are a source of new aerosol particles formed by gas-to-particle conversion (Kulmala et al., 2004, 2013). Boreal forests (also known as taiga) cover approximately 30 % of the world's forests and 8 % of the Earth's surface, so they greatly affect the global radiation budget.

AOPs at SMEAR II have previously been discussed by Virkkula et al. (2011), Zieger et al. (2015), and Pandolfi et al. (2018). Virkkula et al. (2011) presented the scattering and absorption data from a 3-year period (2006–2009), Zieger et al. (2015) presented the hygroscopic properties of AOPs measured during a campaign in May–August in 2013, and Pandolfi et al. (2018) included SMEAR II in the paper on aerosol scattering at 28 ACTRIS stations. At SMEAR II, the study by Pandolfi et al. (2018) involved nephelometer data, from 2006 to 2015, but did not include absorption data.

Long time series (2006–2017) of both scattering and absorption coefficients together at SMEAR II have not been presented before. The aim of this study is to present the characteristics and the temporal variation, especially trends, of AOPs at SMEAR II in this period. We also present the optical properties of particles smaller than 1 μm in diameter (PM_1) that were not presented by either Virkkula et al. (2011) or Pandolfi et al. (2018). To be consistent with the GAW recommendations (WMO/GAW, 2016), we present the results for dry aerosol particles ($\text{RH} < 40 \%$), if not stated otherwise.

2 Measurements and methods

2.1 The boreal research station SMEAR II

The measurements were conducted at SMEAR II (Station for Measuring Ecosystem–Atmosphere Relations; Hari and

Kulmala, 2005). SMEAR II is located in Hytylä, southern Finland ($61^{\circ}51' \text{N}$, $24^{\circ}17' \text{E}$, 181 m above sea level), in the middle of a forest that consists mostly of Scots pine (*Pinus sylvestris* L.) trees (Hari et al., 2013). SMEAR II is classified as a rural measurement station and there are no large pollution sources near the station. The nearest larger cities, Tampere (220 000 inhabitants) and Jyväskylä (140 000 inhabitants), are located about 60 and 100 km from the measurement station. Otherwise, the area is sparsely populated.

2.2 Instrumentation

2.2.1 Measurements of AOPs

The data were measured between 21 June 2006 and 31 December 2017. Measurements of AOPs at SMEAR II started in 2006 for aerosol particles smaller than 10 μm in diameter (PM_{10}). The PM_{10} measurements are sensitive to coarse particles that are typically primary and originated from natural sources, such as soil dust and sea salt. To obtain additional information about submicron particles, parallel measurements of AOPs for PM_1 were launched in June 2010. Motivation to also measure PM_1 particles is that secondary aerosols (both natural and anthropogenic) and anthropogenic primary aerosols are typically submicron particles. Having measurements for different cutoffs also makes the measurements more comparable between different stations since stations might use different cutoff sizes. This is also in line with the GAW recommendation that the aerosol supplied to the nephelometer should be size-segregated to determine the total (< 10 μm diameter) and submicron aerosol light-scattering coefficient (WMO/GAW, 2003).

AOPs are often divided into two different categories: extensive and intensive. Extensive AOPs, such as scattering and absorption coefficients and aerosol optical depth, depend on the number and total volume of particles whereas the intensive AOPs depend on the nature of the aerosol, such as size, shape, and chemical composition. Intensive AOPs describe, for instance, the fraction of aerosol light extinction due to scattering (single-scattering albedo), the wavelength dependence of scattering and absorption (Ångström exponents), and the angular dependence of scattering (hemispheric backscatter fraction) (Ogren, 1995; Sheridan and Ogren, 1999). Intensive properties are calculated from the scattering, backscattering, and absorption measurements at different wavelengths. The backscatter fraction (b) and the Ångström exponent of scattering (α_{sca}) depend on particle size so by measuring the AOPs at different wavelengths we can also obtain indirect information on the size distribution.

The integrating nephelometer measures scattering and backscattering at blue, green, and red wavelengths (450, 550, and 700 nm) and the Aethalometer measures absorption at seven wavelengths ranging from the ultraviolet to the near-infrared (370, 470, 520, 590, 660, 880, and 950 nm). In addition to Aethalometer measurements, parallel measurements

of σ_{abs} with a multi-angle absorption photometer (MAAP, Thermo Scientific model 5012) were started in 2013. Here, absorption data from the AE-31 and scattering data from the TSI3563 were used since they have the longest time series, and an important part of our discussion is the analysis of trends. We used the MAAP data in determining a multiple scattering correction factor for the Aethalometer to obtain more accurate absorption measurements (see Sect. 2.3.2).

Scattering and absorption measurements were recorded at a 5 min resolution before June 2010 and after that with a 10 min resolution. From June 2006 to June 2010, the measurements were conducted for the PM_{10} particles only and since June 2010 also for the PM_1 particles. The sample air was taken through a PM_{10} inlet (Digitel, low-volume PM_{10} inlet) and led alternatingly either directly to the instruments or via an impactor that removes particles larger than 1 μm in diameter. The path of the sample alternated every 10 min.

The aerosol hygroscopic growth is often significant when relative humidity (RH) increases above $\sim 40 \pm 5\%$ and therefore the World Meteorological Organization and Global Atmosphere Watch (WMO and GAW) recommends aerosol monitoring stations to keep sample air RH lower than that (WMO/GAW, 2016). Until March 2010, the integrating nephelometer and the Aethalometer measured sample air that was not dried with any external driers. The sample air was only dried passively by letting it warm from the outdoor temperature to the room temperature (about 22 $^{\circ}\text{C}$). During winter, RH remained below 40 % since the difference between the outdoor and the room temperature was high. In summer, however, the temperature difference was a lot lower. Therefore, sometimes in summer, RH of the sample exceeded the 40 % limit. If the RH was above 40 %, the data were flagged as invalid and omitted from the data analysis, if not stated otherwise. When we discuss dry aerosols, we mean that the measurements were conducted for sample air that had $\text{RH} < 40\%$.

2.2.2 Measurements of aerosol size distribution

To study the causalities between the AOPs and the aerosol size distribution, we included the measurements of aerosol size distribution in our study. The size distributions were measured with a twin differential mobility particle sizer (TDMPS) in the size range 3–1000 nm (Aalto et al., 2001) and a TSI aerodynamic particle sizer (APS, model 3321) in the size range 0.53–10 μm . In the overlapping range of the TDMPS and the APS, we used the number concentrations from the TDMPS up to 700 nm. The TDMPS and APS are located in the same building as the integrating nephelometer and the Aethalometer. The TDMPS and APS had their own individual measurement lines. In the TDMPS measurement line, there was an inlet removing particles larger than 1 μm . There was no active drying system in the TDMPS sample line to prevent particle losses. However, the sheath flows, used in the TDMPS system, were dried ($\text{RH} < 40\%$) so the

particles were sampled in dry conditions. In the APS measurement line there was a pre-impactor that removed particles larger than 10 μm . The APS had its own dryer that heated the sample air to 40 $^{\circ}\text{C}$. This temperature might have evaporated some semivolatile compounds, for instance ammonium nitrate, but this is mainly an issue of urban sites (e.g., Bergin et al., 1997), whereas at the forest site in Hyytiälä low-volatility organic compounds are common (Ehn et al., 2014). Nevertheless, semivolatile aerosol particles are typically secondary particles smaller than 1 μm in diameter so evaporation of them does not have a large effect on the APS measurements.

2.3 Data processing

All the optical data were quality assured manually and averaged for 1 h. All the optical data were converted from ambient conditions to the standard temperature and pressure (STP) conditions (1013 hPa, 0 $^{\circ}\text{C}$). We excluded the data from further analysis if the internal RH in any of the optical instruments exceeded 40 %, if not stated otherwise.

2.3.1 Corrections for the integrating nephelometer data

Both σ_{sca} and σ_{bsca} measured with the nephelometer were corrected for the truncation error according to Anderson and Ogren (1998). The truncation correction uses the Ångström exponent (see Sect. 2.4.1) calculated from the uncorrected data.

Sherman et al. (2015) presented a well-documented analysis for determining the uncertainty of the different AOPs. They determined a total fractional uncertainty of 9.2 % and 8.9 % (8.0 % and 8.1 %) for PM_{10} (PM_1) σ_{sca} and σ_{bsca} .

Generally, in this study, the results are presented for dry aerosol ($\text{RH} < 40\%$), and therefore the hygroscopic growth had no notable effect on scattering. However, we had to take the effect of hygroscopic growth on scattering into account in two special cases: (1) to test if excluding the moist data ($\text{RH} > 40\%$) had a notable effect on the average AOPs and their trends and (2) to calculate the aerosol radiative forcing efficiency (see Sect. 2.4.2) for ambient RH conditions. In these special cases, we used a scattering enhancement factor $f(\text{RH})$ to estimate the effect of RH on scattering. $f(\text{RH})$ describes the increase in σ_{sca} with increasing RH

$$f(\text{RH}) = \frac{\sigma_{\text{sca}}(\text{RH})}{\sigma_{\text{sca}}(\text{RH} = \text{dry})}. \quad (1)$$

$f(\text{RH})$ is the ratio of σ_{sca} measured at high RH and at dry conditions. The $f(\text{RH})$ can be described by the empirical relationship

$$f(\text{RH}) = q \left(1 - \frac{\text{RH}}{100\%} \right)^{-\gamma}, \quad (2)$$

with a parametrization presented by Andrews et al. (2006). They determined mean values for q and γ that were $0.84 \pm$

0.10 and 0.37 ± 0.15 for σ_{sca} and 0.96 ± 0.16 and 0.12 ± 0.15 for σ_{bsca} . Andrews et al. (2006) presented the parameterization at 550 nm so we corrected only the σ_{sca} and σ_{bsca} at the green wavelength. Andrews et al. (2006) used a 4-year-long data set measured at the southern Great Plains near Lamont, in Oklahoma, US. We decided to use this parametrization since they provided the parametrization for both σ_{sca} and σ_{bsca} . Also, the measurements were conducted for continental aerosol, which is closer to aerosols in a boreal forest than the mixtures of pollution, dust, sea salt, and volcanic aerosol, for which Carrico et al. (2003) presented the parametrization for both σ_{sca} and σ_{bsca} . Zieger et al. (2015) determined scattering enhancement at SMEAR II in summer and obtained somewhat different values: $q = 1.01 \pm 0.05$ and $\gamma = 0.25 \pm 0.07$. This would have suited our needs very well, but the q and γ were determined only for σ_{sca} and not for σ_{bsca} , which is why we did not use this parametrization here.

In testing whether excluding the moist data had an effect on the AOPs, we also performed the analysis a data set where we included the periods of high humidity ($\text{RH} > 40\%$) but estimated the moist data ($\text{RH} > 40\%$) to dry conditions by using the $f(\text{RH})$. We also used the $f(\text{RH})$ in calculating the aerosol radiative forcing efficiency in ambient conditions, for which the dry σ_{sca} and σ_{bsca} were converted to ambient RH.

2.3.2 Corrections for the Aethalometer data

The reported flow by the Aethalometer was corrected by comparing the flow with the weekly flow measurements conducted at the station. The correction was applied by using a moving average of these measurements (see Sect. S3.1). An average spot size diameter of 8.3 ± 0.2 mm was measured from the old Aethalometer filters by using a loupe measuring scale magnifier (Eschenbach) with 0.1 mm accuracy and it was used instead of the spot size reported by the Aethalometer.

We corrected the Aethalometer data by using the correction algorithm described by Collaud Coen et al. (2010)

$$\sigma_{\text{abs},i} = \frac{\sigma_{\text{ATN},i} - a_{s,i}\bar{\sigma}_{\text{sca},s,i}}{C_{\text{ref}}L_{s,i}}, \quad (3)$$

where

$$L_{s,i} = \left(\frac{1}{l(1 - \bar{\omega}_{0,s,i}) + 1} - 1 \right) \cdot \frac{\text{ATN}_i}{50\%} + 1, \quad (4)$$

and

$$a_{s,i} = \bar{\zeta}_{\text{sca},s,i}^{d-1} \cdot c \cdot \lambda^{-\bar{\alpha}_{\text{sca},s,i} \cdot (d-1)}. \quad (5)$$

In Eqs. (3)–(5), the subscript i indicates the number of the measurement and the subscript s indicates the average properties of the aerosol particles that are embedded in the filter spot. The parameters with an overbar are the mean values from the start of the filter spot to the i th measurement. In

Eq. (3), the σ_{ATN} is the attenuation coefficient reported by the Aethalometer, a is the scattering correction parameter, C_{ref} is the multiple scattering correction factor, and L is the loading correction function. In Eq. (4), the ω_o is the single-scattering albedo (see Sect. 2.4.1) and the ATN is the light attenuation through the filter spot in percentages. In Eq. (5) the ζ_{sca} is the proportionality constant of the wavelength power-law dependence of σ_{sca} , and α_{sca} is the Ångström exponent of the σ_{sca} (see Sect. 2.4.1). For l , d , and c we used values 0.74, 0.564, and 0.329×10^{-3} , respectively. For scattering correction, we used measured σ_{sca} values that were interpolated and extrapolated to the AE-31 wavelengths. Note that most of the symbols used for the variables are different from those of Collaud Coen et al. (2010). The reason is that in the present work the symbols are used for other variables below.

The C_{ref} was determined by comparing the Aethalometer data, which were corrected only for the filter loading artifact, against the reference absorption coefficient ($\sigma_{\text{abs,ref}}$) measured by the MAAP:

$$C_{\text{ref}} = \frac{\sigma_{\text{ATN}}}{L \cdot \sigma_{\text{abs,ref}}}. \quad (6)$$

The resulted median value for C_{ref} was 3.19, with a standard deviation of 0.67.

The uncertainty of the σ_{ATN} was determined according to Backman et al. (2017)

$$\frac{\delta\sigma_{\text{ATN}}}{\sigma_{\text{ATN}}} = \sqrt{f_A^2 + f_Q^2 + \left(\frac{\delta\sigma_{\text{ATN},\text{zero}} \Delta t_{\text{zero}}}{\sigma_{\text{ATN}} \Delta t_{\text{avg}}} \right)^2}, \quad (7)$$

where the f_A and f_Q are the fractional uncertainties of the Aethalometer spot size and flow, which we determined to be 4.9 % and 1.5 %, respectively; $\delta\sigma_{\text{ATN},\text{zero}}$ is the standard deviation of the zero measurements; Δt_{zero} is the averaging time of the zero measurements; and Δt_{avg} is the averaging time of the measurements. For the uncertainty of σ_{abs} we took into account the fractional uncertainty of the C_{ref} , which was $f_C = 21\%$:

$$\frac{\delta\sigma_{\text{abs}}}{\sigma_{\text{abs}}} = \sqrt{\left(\frac{\delta\sigma_{\text{ATN}}}{\sigma_{\text{ATN}}} \right)^2 + f_C^2}. \quad (8)$$

At 520 nm, the uncertainty of σ_{abs} ranges from 22 % to 24 % if the value of σ_{ATN} varies from 14.2 to 1.3 Mm^{-1} , which are the 10th and 90th percentiles of σ_{ATN} . In this estimation of uncertainty, we did not take the uncertainty of scattering correction into account.

In calculating the single-scattering albedo (see Sect. 2.4.1) and in iterating the complex refractive index (see Sect. 2.4.3), the absorption data had to be interpolated to the same wavelength with the scattering measurements. The absorption data were then interpolated to the blue, green, and red wavelengths (450, 550, and 700 nm), using the Ångström exponent (α) described in Eqs. (11) and (12).

2.4 Data analysis

Here we describe the intensive optical properties, the aerosol radiative forcing efficiency, and parameters derived from the size distribution measurements.

2.4.1 Intensive optical properties

The extensive AOPs, σ_{sca} , σ_{bsa} , and σ_{abs} , were used to calculate intensive properties presented in detail below.

The single-scattering albedo (ω_0) describes how much of the total light extinction (sum of σ_{sca} and σ_{abs}) caused by the aerosol particles is due to scattering:

$$\omega_0 = \frac{\sigma_{\text{sca}}}{\sigma_{\text{sca}} + \sigma_{\text{abs}}}. \quad (9)$$

The ω_0 can be linked to the source and chemical composition of the aerosol particles. High values of ω_0 mean that the aerosol particles are mostly scattering. Particles that have a lower ω_0 have a relatively higher mass fraction of absorbing material, such as soot, which is emitted in combustion processes.

The backscatter fraction (b) describes how much aerosol particles scatter radiation in the backward hemisphere compared with the total scattering:

$$b = \frac{\sigma_{\text{bsca}}}{\sigma_{\text{sca}}}. \quad (10)$$

The angular dependency of particle scattering depends mostly on the particle size. The b is smaller for a size distribution that consists of larger particles since large particles scatter light heavily in the forward direction and thus b can be used as an indicator of the shape of the particle size distribution. The b is an important variable for modeling the direct effect of aerosol particles on the climate since it is used to describe how much sunlight is scattered upwards back into space.

The Ångström exponent (α) is used to describe the wavelength (λ) dependency of a certain optical property (σ) (Ångström, 1929):

$$\alpha = -\frac{\ln \frac{\sigma_1}{\sigma_2}}{\ln \frac{\lambda_1}{\lambda_2}}. \quad (11)$$

After calculating α , the optical property can be extrapolated or interpolated into different wavelengths

$$\sigma_1 = \sigma_2 \left(\frac{\lambda_1}{\lambda_2} \right)^{-\alpha}. \quad (12)$$

In this study, α values were calculated for σ_{sca} and σ_{abs} to obtain α_{sca} and α_{abs} .

Scattering by aerosol particles depends on the relation between the sizes of the particles and the wavelength of the radiation. Therefore α_{sca} is also used as an indicator of the

particle size distribution. The α_{sca} is larger for the smaller particles since they have a stronger wavelength dependency. If the value of α_{sca} is larger than 2, the volume distribution is typically dominated by particles smaller than 0.5 µm. If the parameter α_{sca} is smaller than 1, larger particles (physical diameter $D_p > 0.5 \mu\text{m}$) predominate in the distribution (Schuster et al., 2006). In comparison to b , α_{sca} is more sensitive to the coarse-mode particles (e.g., Collaud Coen et al., 2007). However, for multimodal size distributions this relationship is not quite unambiguous, as discussed by, for example, Schuster et al. (2006) and Virkkula et al. (2011).

The α_{abs} also depends on the chemical composition, coating, and size of the particles, even though the chemical composition is generally considered to be a more important factor. The α_{abs} is usually used to identify black carbon (BC) and brown carbon (BrC) particles. The BC particles absorb radiation effectively at all wavelengths; the BrC particles, which consist of organic carbon compounds, absorb light strongly at shorter wavelengths, but not at longer wavelengths. If the particles consist purely of BC, the absorption would have a wavelength dependency of approximately λ^{-1} , and α_{abs} would be equal to unity. However, if the particles also consist of material that absorbs light only at ultraviolet wavelengths, α_{abs} would be larger than 1. In aging processes, the BC particles may become coated by some purely scattering material, such as sulfuric acid or ammonium sulfate, or by slightly absorbing organic material (Schnaiter et al., 2005; Zhang et al., 2008). The coating greatly affects the absorption wavelength dependency, and thus the division into BC and BrC by considering only the α_{abs} is not that simple. If the sizes of the BC particles and the thickness and complex refractive index (m) of the coating are not known, it is challenging to use α_{abs} to describe the chemical composition of the particles (Gyawali et al., 2009; Lack and Cappa, 2010). In spite of the fact that α_{abs} also depends on the coating, the absorption wavelength dependency is often used to describe the source of the BC (Sandradewi et al., 2008; Zotter et al., 2017). The source apportionment assumes that there are BC emissions only from traffic and wood burning and that the BC from these sources has a specific wavelength dependency.

The estimated uncertainties for the intensive AOPs are presented in Sect. S4 in the Supplement. The uncertainties were calculated according to Sherman et al. (2015).

2.4.2 Aerosol radiative forcing efficiency

To investigate how the AOPs at SMEAR II would affect the climate, the aerosol radiative forcing efficiency ($\Delta F \delta^{-1}$ or RFE) was calculated. The RFE is a simplified formula that describes how large a difference the aerosol particles would make to the radiative forcing (ΔF or RF) per unit of aerosol

optical depth (δ) (Sheridan and Ogren, 1999):

$$\frac{\Delta F}{\delta} = -DS_0T_{\text{at}}^2\omega_0\beta(1-A_C) \left[(1-R_S)^2 - \left(\frac{2R_S}{\beta}\right)\left(\frac{1}{\omega_0}-1\right) \right]. \quad (13)$$

RFE does not take into account that the properties and number of aerosol particles vary vertically in the atmospheric column. In Eq. (13), D is the fractional day length, S_0 the solar constant, T_{at} the atmospheric transmission, A_C the fractional cloud amount, and R_S the surface reflectance for which the following global average values were used, respectively: $D = 0.5$, $S_0 = 1370 \text{ W m}^{-2}$, $T_{\text{at}} = 0.76$, $A_C = 0.6$, and $R_S = 0.15$. The global averages do not represent the conditions at SMEAR II and the RFE calculated by using these constants is probably not realistic for the regional area. However, using the global averages makes it possible to compare the reported aerosol properties between different stations around the world. The values were chosen according to Haywood and Shine (1995), who used these values independently of wavelength in calculating the RF. Sheridan and Ogren (1999) used these same constants later in calculating the RFE at 550 nm and in this study we also determine the RFE at 550 nm. The factor β is the upscatter fraction and is calculated by using the b (Delene and Ogren, 2002):

$$\beta = 0.0817 + 1.8495b - 2.9682b^2. \quad (14)$$

It must be noted that Eq. (14) does not take into account the variation in the sun's zenith angle.

As stated by Sherman et al. (2015), the purpose of determining the RFE is to provide means for comparing the intrinsic aerosol forcing efficiency of aerosols measured at different sites. We calculated the RFE by using the same constant values to have results comparable with other studies in very different types of environments (e.g., Sheridan and Ogren, 1999; Andrews et al., 2011; Sherman et al., 2015; Shen et al., 2018) and to study how the RFE changes with varying ω_0 and b . We refer to the RFE that was calculated by using the abovementioned constant values as $\text{RFE}_{\text{H\&S}}$. It must be noted that ω_0 and b used in Eq. (13) are defined for dried sample air and therefore $\text{RFE}_{\text{H\&S}}$ does not represent ambient conditions. In the ambient air, RH is larger and the AOPs are different due to hygroscopic growth.

In addition to $\text{RFE}_{\text{H\&S}}$, we calculated a seasonal RFE by allowing the D to vary and by using more realistic seasonal values for A_C and R_S . The seasonal variations in these parameters are presented in Fig. S1. We refer to the seasonal RFE as RFE_S . The effect of ambient RH on ω_0 and b , and hence on RFE, was also studied. The seasonal RFE calculated for ambient RH is referred to as $\text{RFE}_{S,\text{moist}}$.

Seasonal A_C was derived by using ceilometer data. The ceilometer was deployed at the Halli airport (about 25 km from SMEAR II) by the Finnish Meteorological Institute (FMI) in 2010. The data were averaged for each month to

obtain a seasonal variation. The lowest mean of A_C occurred in July (~ 0.25) and the highest mean occurred in January (~ 0.76).

For the seasonal R_S , reflectivity determined by Kuusinen et al. (2012) was used. They determined the R_S in a boreal forest for different amounts of canopy snow cover. According to the FMI, the average season of snow cover in Hyytiälä is from 16 November to 20 April (FMI: <http://ilmatieteenlaitos.fi/lumitilastot>, in Finnish only, last access: 13 March 2019) and for that time period we used $R_S = 0.314 \pm 0.14$ that Kuusinen et al. (2012) determined as the average albedo for a snow-covered canopy. For snow-free forest we used $R_S = 0.126$, which is an average of the mean monthly albedos Kuusinen et al. (2012) determined for snow-free months.

In calculating the ω_0 and b in ambient conditions, we used the equations and parametrization presented in Sect. 2.3.1 to convert the σ_{sca} and σ_{bsca} to ambient RH; σ_{abs} was assumed to be constant with increasing RH, as Nessler et al. (2005) showed that the change in the σ_{abs} with increasing RH is very small compared to scattering. The seasonally averaged RH was determined from RH measurements conducted at the height of 16 m. The lowest mean RH occurred in May ($\sim 62\%$) and the highest in November ($\sim 95\%$).

More information about the seasonal D , A_C , R_S , and RH can be found in the Supplement Sect. S2.

2.4.3 Properties calculated from particle size distribution

Size distributions were used to calculate differently weighted mean diameters. In this study, we used the geometric mean diameter (GMD) and the volume mean diameter (VMD). The GMD is the mean diameter that is weighted by the number concentration (N)

$$\text{GMD} = \exp\left(\frac{\sum N_i \ln D_{p,i}}{\sum N_i}\right), \quad (15)$$

and the VMD is weighted by the particle volume (V)

$$\text{VMD} = \frac{\sum D_{p,i} V_i}{V_{\text{tot}}} = \frac{\sum N_i D_{p,i}^4}{\sum N_i D_{p,i}^3}. \quad (16)$$

Since the particle number concentrations are the highest for the nucleation and Aitken modes, the GMD describes the distribution changes in the smallest sizes. The VMD, in contrast, is affected by the changes in the accumulation and coarse mode since they contribute the most to the volume size distribution.

The measurements of the AOPs and size distribution can be combined to determine the complex refractive index ($m = n + ik$) that describes how much the particles scatter and absorb light. The m can be used to model σ_{sca} , σ_{bsca} , and σ_{abs} from the size distribution. The m consists of the real part (n), which accounts for the scattering, while the absorption is described by the imaginary part (k). Like ω_0 , m provides information on the chemical composition of the aerosol particles.

In this study, m was iterated from the σ_{sca} , σ_{abs} , and size distribution measurements in a manner similar to that described by Virkkula et al. (2011). In the first step of the interpolation $\sigma_{\text{sca},\text{Mie}}$ and $\sigma_{\text{abs},\text{Mie}}$, which are the modeled scattering and absorption coefficients, were determined for the measured size distribution by using the Mie theory with initial $m = 1.544 + 0.019i$. The $\sigma_{\text{sca},\text{Mie}}$ and $\sigma_{\text{abs},\text{Mie}}$ were then compared with the measured σ_{sca} and σ_{abs} . If the calculated and measured values did not agree, the real part of m was first varied stepwise by 0.001 until the measured and modeled σ_{sca} agreed. Next, the imaginary part of m was varied in the same way until the measured and modeled σ_{abs} agreed. This iteration was continued until the measured and calculated values agreed within 1 %. The new imaginary part of m also affected σ_{sca} so the real part had to be reiterated. The MATLAB codes developed by Mätzler (2002) were used to model the Mie scattering and absorption.

2.4.4 Long-term trend analysis

Over the whole measurement period, 81 % of the nephelometer data and 70 % of the Aethalometer data were considered valid. All of the AOPs had some gaps in the data (see Fig. 4). More detailed monthly data coverages of σ_{sca} and σ_{abs} are presented in Table S1 of the Supplement. Most of the gaps in the time series of the AOPs during the summers of 2006 to 2010 were due to too high RH. If the moist data were included, the overall data coverage would increase to 89 % and 77 % for scattering and absorption data, respectively. After the installation of the Nafion dryers in March 2010, the humidity caused no further problems. The gap in 2010 was due to maintenance and installation of the dryers and the switching inlet system. Some additional σ_{bsca} data were missing, due to malfunction of the backscatter shutter of the integrating nephelometer. Dirty optics, malfunctions, and maintenance caused the gaps in the σ_{abs} data in 2012 and 2015.

All the months that had at least 14 d of valid data were included in the long-term trend analysis. The trends and their significance were determined using the seasonal Kendall test described by Gilbert (1987). This test determines if there is a similar trend for each season (month) separately. All of the trends were calculated for the monthly medians, and at least 14 d of valid data in a given month were required for this month to be taken into account in the trend analysis.

3 Results and discussion

Below, we present the descriptive statistics of the AOPs, their seasonal variations, and long-term trends at SMEAR II. The figures of the AOPs in this section are presented in the green wavelength (550 nm for the scattering and intensive properties and 520 nm for the absorption measurements). In the figures of α_{sca} and α_{abs} , wavelength ranges of 450–700 and

370–950 nm were used. The results are presented for dry aerosols ($\text{RH} < 40 \%$), if not stated otherwise.

3.1 Characterization of boreal aerosol particles

The descriptive statistics of the AOPs of both the PM_{10} and PM_1 particles are shown in Tables 1 and 2. The statistics are calculated from hourly data. Tables 1 and 2 show that for most of the variables the mean and the median values were quite different, which means that the data were not normally distributed. Therefore, we use the medians, which are not as sensitive to extreme values as the mean, to describe the characteristics of the AOPs.

The median values of PM_{10} σ_{sca} and σ_{abs} at SMEAR II at the green wavelength were 9.8 and 1.4 Mm^{-1} . In comparison to similar studies conducted at other Finnish measurement stations at Pallas in northern Finland (Lihavainen et al., 2015) and at Pujo tower in Kuopio, eastern Finland (Leskinen et al., 2012), results at SMEAR II showed the highest σ_{sca} and σ_{abs} for PM_{10} particles. At SMEAR II, the median value of σ_{sca} was about 2 times higher and the value of σ_{abs} more than 3 times higher than at Pallas, where the median $\sigma_{\text{sca}} = 4.4$ and $\sigma_{\text{abs}} = 0.4 \text{ Mm}^{-1}$ were measured at the green wavelength. The Pallas station is remote, located 170 km north of the Arctic Circle, far from anthropogenic sources, which explains the low concentrations. At SMEAR II, parameters σ_{sca} and σ_{abs} were about 1.4 and 1.1 times higher than that measured at the Pujo tower, where the median values of $\sigma_{\text{sca}} = 7.2$ and $\sigma_{\text{abs}} = 1.0 \text{ Mm}^{-1}$ were measured at the green and red wavelengths, respectively. Pujo tower is a semi-urban measurement station located only 2 km away from the Kuopio city center. At the Pujo tower, the measurements were conducted only on particles smaller than $2.5 \mu\text{m}$, which explains part of the differences, at least for σ_{sca} .

Even though the σ_{sca} measured at SMEAR II is high compared to other measurements conducted in Finland, the air measured at SMEAR II is still clean when compared to European sites. Due to the remote location, Pandolfi et al. (2018) observed low σ_{sca} at SMEAR II compared to other European sites. Lower median σ_{sca} values were observed only in the arctic region, at another Nordic rural station in Birkenes, Norway, and at several high mountain sites. The highest median $\sigma_{\text{sca}} (> 40 \text{ Mm}^{-1})$ was observed by Pandolfi et al. (2018) at urban and regional sites in central and eastern Europe.

From Table 1 we see that the PM_{10} AOPs differ somewhat from the results of Virkkula et al. (2011) and Pandolfi et al. (2018), which can be explained by the trends and by differences in the data processing. For example the median value of $\sigma_{\text{sca}} (\sim 10 \text{ Mm}^{-1})$ at $\lambda = 550 \text{ nm}$ in this study was lower than that presented by Virkkula et al. (2011) ($\sim 12 \text{ Mm}^{-1}$) and by Pandolfi et al. (2018) ($\sim 11 \text{ Mm}^{-1}$), which is probably due to the tendency of σ_{sca} to decrease (see Sect. 3.2). Another reason is that in the data processing Virkkula et al. (2011) used the earlier WMO and GAW rec-

Table 1. Descriptive statistics of the AOPs for the PM₁₀ particles. The average values were calculated from all valid data.

PM ₁₀	λ (nm)	Mean \pm SD	1 %	10 %	25 %	50 %	75 %	90 %	99 %
σ_{sca} (Mm ⁻¹)	450	21.8 \pm 23.3	1.8	4.5	7.6	14.2	26.8	48.5	114.1
	550	15.2 \pm 16.7	1.3	3.4	5.5	9.8	18.3	33.4	82.5
	700	9.5 \pm 10.5	0.8	2.3	3.7	6.3	11.3	20.3	52.3
σ_{bsca} (Mm ⁻¹)	450	2.5 \pm 2.9	0.2	0.6	1.0	1.8	3.2	5.3	11.1
	550	2.0 \pm 1.8	0.2	0.5	0.8	1.4	2.5	4.2	8.8
	700	1.6 \pm 1.5	0.2	0.4	0.7	1.2	2.0	3.4	7.4
σ_{abs} (Mm ⁻¹)	370	3.0 \pm 3.6	0.2	0.6	1.0	1.9	3.6	6.6	18.1
	470	2.5 \pm 2.9	0.2	0.5	0.8	1.6	3.0	5.4	14.3
	520	2.2 \pm 2.4	0.1	0.4	0.7	1.4	2.6	4.7	12.3
	590	1.9 \pm 2.2	0.1	0.4	0.7	1.3	2.4	4.2	10.8
	660	1.8 \pm 2.0	0.1	0.3	0.6	1.2	2.2	3.8	9.9
	880	1.3 \pm 1.4	0.1	0.3	0.5	0.9	1.6	2.9	7.2
	950	1.2 \pm 1.3	0.1	0.3	0.4	0.8	1.5	2.6	6.5
ω_0	450	0.88 \pm 0.07	0.64	0.80	0.85	0.89	0.93	0.95	0.98
	550	0.87 \pm 0.07	0.62	0.78	0.84	0.88	0.92	0.94	0.98
	700	0.84 \pm 0.08	0.55	0.74	0.80	0.85	0.90	0.93	0.97
b	450	0.13 \pm 0.03	0.08	0.10	0.11	0.12	0.14	0.16	0.21
	550	0.14 \pm 0.03	0.09	0.11	0.13	0.14	0.16	0.17	0.21
	700	0.19 \pm 0.07	0.07	0.13	0.15	0.18	0.21	0.25	0.44
α_{sca}	450/550	1.73 \pm 0.52	0.23	1.03	1.49	1.82	2.09	2.29	2.58
	450/700	1.80 \pm 0.55	0.32	1.00	1.53	1.88	2.17	2.39	2.80
	550/700	1.85 \pm 0.64	0.23	0.95	1.53	1.95	2.26	2.50	3.15
α_{abs}	370/520	0.95 \pm 0.48	-0.29	0.51	0.76	0.98	1.16	1.32	1.97
	370/950	0.95 \pm 0.36	-0.16	0.55	0.80	0.99	1.13	1.24	1.69
	470/660	0.95 \pm 0.49	-0.52	0.52	0.80	1.01	1.15	1.29	2.07
	470/950	0.99 \pm 0.41	-0.32	0.58	0.86	1.06	1.18	1.28	1.83
	660/950	1.02 \pm 0.57	-0.77	0.57	0.90	1.11	1.23	1.34	2.17
n	450	1.541 \pm 0.065	1.330	1.478	1.512	1.542	1.572	1.607	1.697
	550	1.518 \pm 0.067	1.289	1.452	1.490	1.522	1.550	1.581	1.674
	700	1.491 \pm 0.091	1.247	1.379	1.454	1.501	1.536	1.574	1.740
k	450	0.021 \pm 0.020	0.002	0.006	0.009	0.016	0.026	0.039	0.097
	550	0.020 \pm 0.018	0.002	0.006	0.010	0.016	0.025	0.038	0.089
	700	0.022 \pm 0.019	0.003	0.007	0.011	0.018	0.027	0.041	0.092
RFE _{H&S} (W m ⁻²)	550	-22 \pm 6	-32	-28	-26	-23	-19	-16	-3
RFE _S (W m ⁻²)	550	-35 \pm 32	-97	-82	-67	-26	-5	0	12
RFE _{S,moist} (W m ⁻²)	550	-33 \pm 28	-88	-74	-62	-24	-5	-2	4

ommendation (WMO/GAW, 2003) and used data measured at RH < 50 % and did not perform any RH corrections.

We also determined a strong tendency for σ_{abs} to decrease as well, and the median value of σ_{abs} ($\sim 1.3 \text{ Mm}^{-1}$, interpolated to 550 nm) was somewhat lower than the median ($\sim 1.5 \text{ Mm}^{-1}$, at 550 nm) in the study by Virkkula et al. (2011). However, the observed σ_{abs} values between these two studies are not fully comparable due to the differences in the Aethalometer data processing. Virkkula et al. (2011) reported no flow or spot size corrections and they used the algo-

rithm of Arnott et al. (2005) and $C_{\text{ref}} = 3.688$ at $\lambda = 520 \text{ nm}$. Naturally, the different methods used in the absorption data processing also affected the optical properties that are dependent on the σ_{abs} , such as ω_0 and k . In the correction algorithm by Arnott et al. (2005), the C_{ref} is wavelength dependent, which increases the α_{abs} . Virkkula et al. (2011) reported a median value of $\alpha_{\text{abs}} = 1.4$ that is notably higher than the median value of $\alpha_{\text{abs}} = 1.0$ determined by our study. The difference in parameter α_{abs} is attributed to the correction algorithm since in the present work the median value

Table 2. Descriptive statistics of the AOPs for the PM₁ particles. The average values were calculated from all valid data; therefore if compared with the PM₁₀ average values, there is a 4-year-shorter data set.

PM ₁	λ (nm)	Mean \pm SD	1 %	10 %	25 %	50 %	75 %	90 %	99 %
σ_{sca} (Mm ⁻¹)	450	17.7 \pm 19.2	1.2	3.1	5.6	11.3	22.3	40.4	96.1
	550	11.4 \pm 13.0	0.8	2.1	3.6	7.1	14.1	26.1	64.8
	700	6.3 \pm 7.5	0.4	1.2	2.0	3.8	7.6	14.4	37.4
σ_{bsca} (Mm ⁻¹)	450	2.1 \pm 2.0	0.2	0.4	0.8	1.4	2.7	4.5	9.7
	550	1.6 \pm 1.5	0.1	0.3	0.6	1.1	2.0	3.4	7.5
	700	1.2 \pm 1.2	0.1	0.3	0.5	0.8	1.5	2.6	5.9
σ_{abs} (Mm ⁻¹)	370	2.4 \pm 2.9	0.1	0.4	0.8	1.6	2.9	5.2	15.0
	470	2.0 \pm 2.3	0.1	0.4	0.7	1.3	2.4	4.3	11.7
	520	1.7 \pm 1.9	0.1	0.3	0.6	1.2	2.1	3.7	10.0
	590	1.6 \pm 1.7	0.1	0.3	0.5	1.0	1.9	3.3	8.8
	660	1.4 \pm 1.6	0.1	0.3	0.5	0.9	1.8	3.1	8.0
	880	1.1 \pm 1.1	0.1	0.2	0.4	0.7	1.3	2.3	5.8
	950	0.9 \pm 1.0	0.0	0.2	0.3	0.6	1.2	2.0	5.1
ω_0	450	0.88 \pm 0.08	0.62	0.78	0.84	0.89	0.93	0.96	0.98
	550	0.85 \pm 0.08	0.59	0.75	0.81	0.87	0.91	0.94	0.98
	700	0.80 \pm 0.10	0.48	0.67	0.75	0.81	0.87	0.91	0.96
b	450	0.13 \pm 0.03	0.07	0.10	0.11	0.13	0.14	0.17	0.23
	550	0.15 \pm 0.03	0.09	0.12	0.13	0.15	0.17	0.19	0.24
	700	0.23 \pm 0.13	-0.06	0.14	0.17	0.21	0.26	0.34	0.78
α_{sca}	450/700	2.22 \pm 0.44	0.88	1.70	1.99	2.28	2.51	2.66	2.95
	450/550	2.36 \pm 0.55	0.74	1.76	2.09	2.41	2.66	2.87	3.70
	550/700	2.48 \pm 0.81	0.25	1.73	2.16	2.52	2.82	3.13	4.69
α_{abs}	370/520	0.96 \pm 0.61	-0.67	0.47	0.74	0.99	1.20	1.39	2.32
	370/950	0.97 \pm 0.44	-0.36	0.52	0.80	1.03	1.19	1.33	1.96
	470/660	0.94 \pm 0.66	-0.94	0.46	0.76	1.00	1.17	1.33	2.35
	470/950	1.03 \pm 0.51	-0.51	0.56	0.87	1.11	1.25	1.39	2.24
	660/950	1.13 \pm 0.72	-1.10	0.60	0.97	1.20	1.35	1.54	2.96
n	450	1.509 \pm 0.057	1.348	1.441	1.478	1.513	1.542	1.568	1.634
	550	1.484 \pm 0.054	1.338	1.422	1.456	1.487	1.516	1.540	1.598
	700	1.471 \pm 0.074	1.294	1.393	1.435	1.472	1.505	1.537	1.677
k	450	0.025 \pm 0.020	0.003	0.008	0.013	0.020	0.031	0.045	0.099
	550	0.025 \pm 0.018	0.004	0.009	0.014	0.021	0.031	0.044	0.093
	700	0.028 \pm 0.019	0.005	0.011	0.017	0.024	0.035	0.049	0.098

of $\alpha_{\text{abs}} = 1.34$ for the wavelength range 370–950 when the Arnott et al. (2005) algorithm is used (see Table S2).

The differences between the AOPs of the PM₁ and PM₁₀ particles are explained by the differences in concentrations, size distributions, and chemical compositions. If only the PM₁₀ data overlapping with the PM₁ measurements were taken into account, the median values of PM₁₀ σ_{sca} , σ_{abs} , ω_0 , b , α_{sca} , α_{abs} , n , and k would have been 9.6 Mm⁻¹, 1.3 Mm⁻¹, 0.89, 0.14, 1.92, 0.97, 1.525, and 0.014 (σ_{sca} , ω_0 , b , α_{sca} , n , and k at 550 nm, σ_{abs} at 520 nm). For PM₁ the median values were 7.1 Mm⁻¹, 1.2 Mm⁻¹, 0.87, 0.15, 2.41, 1.03, 1.487, and 0.021. The extensive variables (σ_{sca} , σ_{bsca} , and σ_{abs}) were smaller for the PM₁ measurements since there was less parti-

cle volume interacting with the radiation. The α_{sca} and b are related to the sizes of the particles, so they were naturally different between the PM₁ and PM₁₀ particles. For the smaller PM₁ particles, the α_{sca} and b were larger than for the PM₁₀ particles. However, b does not have as large a difference between the PM₁ and PM₁₀ particles as α_{sca} .

On average submicron particles caused about 75 % of the total scattering of the PM₁₀ particles. This was apparently a lower fraction than in the previous analysis of SMEAR II scattering data. Virkkula et al. (2011) stated that the average contributions of submicron particles to the total σ_{sca} was in the range of 88 %–92 %, clearly more than in the present work. However, in that study the scattering size dis-

tribution and the contributions of the various size ranges were calculated from particle number size distributions with a Mie model and the physical diameters (D_p) were used, whereas here the PM₁ corresponds to particles smaller than the aerodynamic diameter D_a of 1 µm. With a particle density of 1.7 g cm⁻³ this corresponds to the physical diameter $D_p = (1/1.7)^{1/2}$ 1 µm ≈ 0.77 µm. The contribution of particles smaller than 0.77 µm is approximately 85 % if it is estimated from Fig. 11 of Virkkula et al. (2011), still more than the ~ 75 % contribution of submicron scattering shown here. This may have resulted from the cutoff diameter of the PM₁ impactor not being exactly sharp and also because the particles entering the impactor may have still been somewhat moist and thus larger than their dry size and were therefore removed from the sample stream. Further analysis of the difference is omitted here.

The PM₁ particles absorbed about 90 % of the total PM₁₀ particle absorption. So for the σ_{abs} there were no large differences in the σ_{abs} of the PM₁ and PM₁₀ particles. The coarse-mode particles are typically primary and they have a quite high ω_0 so their absorption is minor compared with the PM₁ particles. The soot particles, which account for most of the particulate absorption, are typically submicron particles. Due to the relative differences in the scattering and absorption, the median ω_0 and n were lower for the PM₁ particles than PM₁₀ particles.

3.1.1 Seasonality of AOPs

The seasonal variation in the PM₁₀ AOPs was clearly visible in the 11.5-year record shown in Fig. 1. The seasonal variations in σ_{sca} and σ_{bsca} (Fig. 1a and b) were not yet as clear in Virkkula et al. (2011) as they are now. For the σ_{sca} and σ_{bsca} , two local maxima occurred during late winter (February) and late summer (July). The local minima occurred during spring (April) and late autumn (October). The σ_{abs} showed the highest values during winter (February) and the lowest values during summer (June). Part of this variation is explained by boundary layer dynamics. In summer, the boundary layer is higher and well mixed, therefore diluting the aerosol concentration, and in winter the situation is the opposite and the pollution accumulates in the shallow boundary layer. Also, the sources of aerosol particles vary seasonally, which affects the seasonal concentrations.

For the extensive properties, the highest values occurred at the same time in winter (February) when the ω_0 was also low, which indicates that there were larger numbers of particles from anthropogenic sources than in summer. Hyvärinen et al. (2011) observed increased equivalent black carbon (eBC, meaning optically measured BC) concentration at SMEAR II in winter, when the long-range transport brings pollution from central and eastern Europe. However, Hienola et al. (2013) estimated that about 70 % of the measured eBC at SMEAR II is emitted from local or regional sources or transported from Finnish cities, so the local and regional emis-

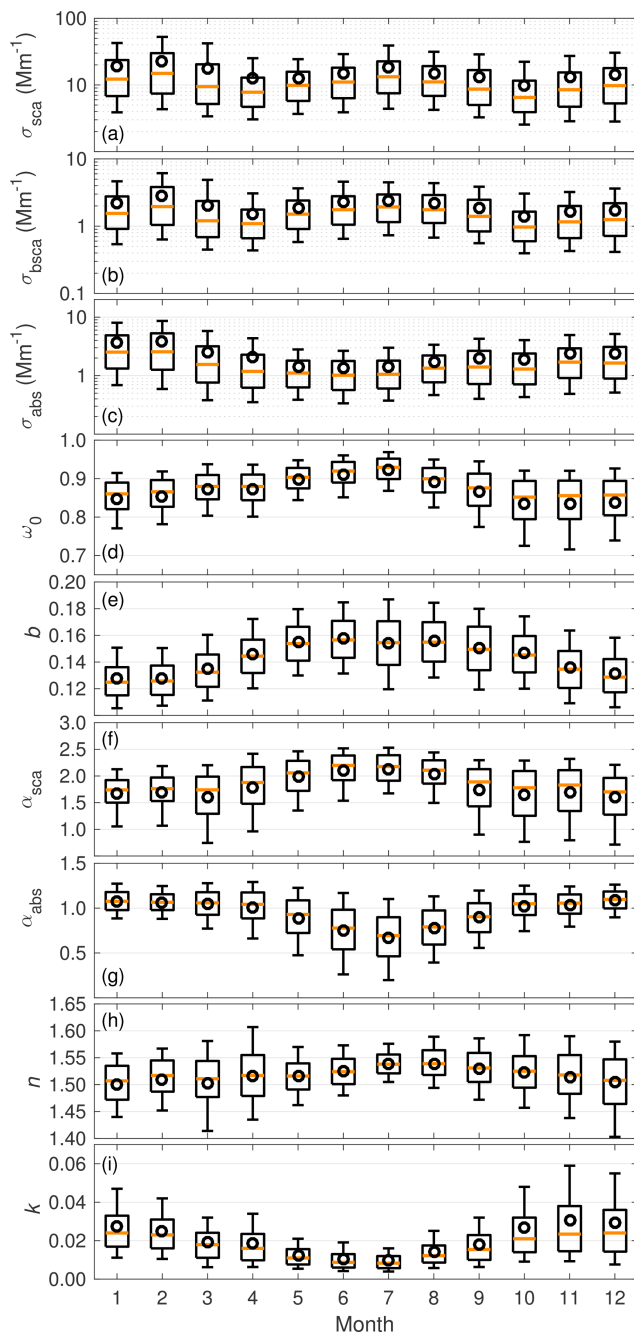


Figure 1. Seasonal variation in the aerosol optical properties for PM₁₀ particles. The boxes represent the 25th and 75th percentiles and the whiskers the 10th and 90th percentiles of the data. The orange line is the median and the mean is presented with a black circle.

sions also have a significant role in the elevated eBC concentration. Since February is one of the coldest months in Finland, domestic wood burning in local and regional areas increases the particle concentration (Karvosenoja et al., 2011). Pollution can also be transported from nearby cities (the largest and closest are Tampere and Jyväskylä). Hyvärinen

et al. (2011) observed no remarkable changes in the Hyytiälä eBC concentration coming from the Tampere region. However, the largest concentrations they observed came from the direction of Orivesi, a small town (population about 9000) 20 km from the measurement station.

The α_{abs} is typically associated with the source of the BC and it is often used to quantify whether the BC is traffic or wood burning related (Sandradewi et al., 2008; Zotter et al., 2017) so that high α_{abs} is a sign of wood burning. In the source apportionment, α_{abs} close to 1 indicates that the BC is from traffic-related sources. Since we observed relatively higher α_{abs} in winter, the results are in line with the assumption of domestic wood burning that takes place during winter. However, in summer, α_{abs} was often < 1 , which would yield an unphysical fraction (over 100 %) of traffic-related BC. Values below 1 could have been caused by large BC particles ($D_p > 100 \text{ nm}$) that have a purely scattering coating (Lack and Cappa, 2010). It must be noted that the α_{abs} also depends on the correction algorithm. For example, if the σ_{abs} were corrected with the algorithm proposed by Arnott et al. (2005), the median value of α_{abs} would have been 1.34 ± 0.51 (see Table S2). Using the α_{abs} , which was determined by using the correction by Arnott et al. (2005), the results for the source apportionment would be different and they would show a higher fraction of BC from wood burning.

The α_{abs} is also used to describe the chemical properties of the particles. Higher α_{abs} indicates that light is absorbed not only by BC, but also by some light-absorbing organic carbon compounds, i.e., brown carbon (BrC). In using only α_{abs} , it is difficult to determine if the particles consist of BrC since BC particles with a coating can also reach α_{abs} values up to 1.6 (Lack and Cappa, 2010). In Fig. 1g we can see that the value of 1.6 is not really reached at SMEAR II if the correction algorithm by Collaud Coen et al. (2010) was used. Since α_{abs} is dependent on the size of the BC core, the thickness of the coating and the m of the coating, further investigation of its complex nature is omitted here.

In summer, the ω_0 had its highest values since the parameter σ_{sca} was high and the parameter σ_{abs} was low. High σ_{sca} but low σ_{abs} suggests that the anthropogenic influence was not strong in summer and that there was higher contribution of particles from natural sources when the vegetation was active and growing. The scattering maximum in summer was probably caused by secondary organic particles (Tunved et al., 2006).

The seasonal variation in α_{sca} and b depends on the seasonal variation in the size distribution of the particles. Both α_{sca} and b were maximal in summer and minimal in winter, suggesting that in summer, the particle population consisted of smaller particles than in winter. A trajectory analysis by Virkkula et al. (2011) showed that the highest α_{sca} originated within a $\sim 200 \text{ km}$ radius around the station, which means that the smallest particles were rather freshly emitted. This supports the hypothesis that in summer a high fraction of the aerosols are secondary organic particles.

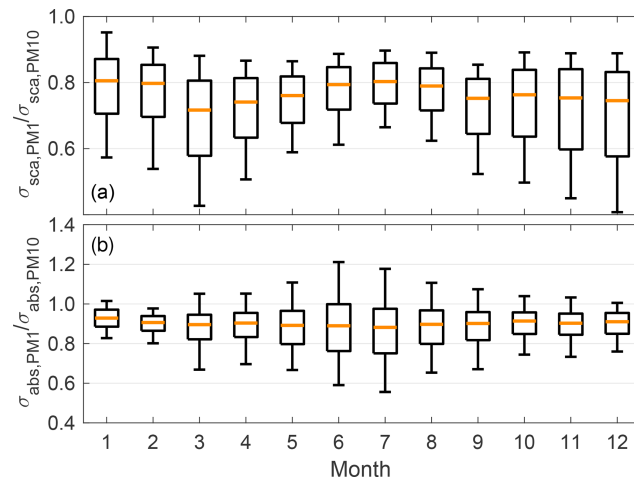


Figure 2. Seasonal variation in the $\text{PM}_1 / \text{PM}_{10}$ ratio for (a) σ_{sca} and (b) σ_{abs} . The explanation for the boxplots are the same as in Fig. 1.

The impact of smaller particles in summer, indicated by the high α_{sca} and b , is also seen in Fig. 2a, which presents the seasonal variation in the $\sigma_{\text{sca}} \text{PM}_1 / \text{PM}_{10}$ ratio. The ratio describes the fraction of fine particles (PM_1) on the $\text{PM}_{10} \sigma_{\text{sca}}$ and it shows that, in addition to summer, the fine particles also have a high impact in winter, which was not seen in α_{sca} and b variation. Closer investigation on the seasonally averaged size distributions, which are presented in Fig. 3 (and S5), reveal that the seasonal variations in α_{sca} and b are more dependent on the shifts in the accumulation mode than in the coarse mode. Figure 3 shows that in winter, the VMD_{tot} had its minimum due to a lack of coarse particles. This is in contrast with the observation of smaller α_{sca} and b , but it supports the maximum we see in the $\sigma_{\text{sca}} \text{PM}_1 / \text{PM}_{10}$ ratio. The seasonal variations in α_{sca} and b were then explained by the seasonal variation in volumetric mean diameter calculated for particles smaller than $1 \mu\text{m}$ (VMD_{fine}). VMD_{fine} is a good indicator for the shifting accumulation mode and it is not affected by the coarse mode. In winter, when the α_{sca} and b were small, the accumulation mode was shifted towards larger sizes and the median of VMD_{fine} was about 350 nm. In summer, when the α_{sca} and b had their maxima, the situation was the opposite and VMD_{fine} was smaller, about 250 nm.

The seasonal variation in the size distribution did not affect the $\sigma_{\text{abs}} \text{PM}_1 / \text{PM}_{10}$ ratio and the median of the ratio did not vary seasonally, which is shown in Fig. 2b. However, the deviation of the $\sigma_{\text{abs}} \text{PM}_1 / \text{PM}_{10}$ ratio had a clear seasonal variation. In summer, the variation was considerably higher than in winter. In the correction algorithm, which was used for the absorption data (Eq. 3), part of the σ_{sca} is subtracted from σ_{abs} as an apparent absorption (Müller et al., 2011). The subtraction of σ_{sca} causes relatively high uncertainty when the σ_{abs} is low and σ_{sca} is high, like it is in summer. This uncertainty is emphasized for PM_{10} measurements since the σ_{sca}

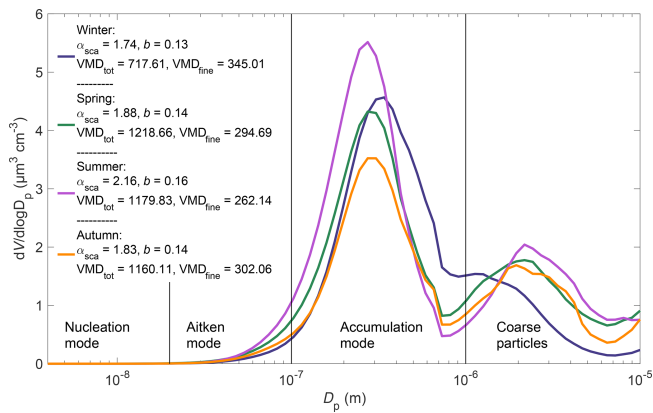


Figure 3. Mean size distribution for winter (December–February), spring (March–May), summer (June–August), and autumn (September–November). Also, the average α_{sca} , b , VMD_{tot} , and VMD_{fine} for the seasons are presented in the figure. VMD_{tot} and VMD_{fine} are reported in nm.

is relatively higher than σ_{abs} , if compared to PM₁ measurements. The uncertainty in the measurements also explains why many values were above 1 in the PM₁ / PM₁₀ σ_{abs} ratio.

3.2 Long-term trends of the AOPs

The about 11.5-year-long time series of the PM₁₀ AOPs were used to determine long-term trends. For a comparison, we also conducted the trend analysis for the PM₁ data, which had shorter, about 7.5-year-long, time series. It must be noted that trends for shorter time series are more sensitive to the year-to-year variability and must be interpreted with caution. The slopes of the trends and the trend statistics are presented in Table 3. The table also presents the trends as percentages, which were calculated by dividing the slope by the overall median value of the variable. The trends are also plotted in Fig. 4, where the monthly medians of the PM₁₀ AOPs at SMEAR II used in this analysis are presented. The monthly medians are included in Fig. 4 only if the month had at least 14 d of valid data.

In all the extensive properties, the trends were negative. The slopes of the trends for PM₁₀ σ_{sca} , σ_{bsca} , and σ_{abs} were -0.32 , -0.038 , and $-0.086 \text{ Mm}^{-1} \text{ yr}^{-1}$, respectively. The decrease in the extensive properties was due to a decrease in the total particle number concentration (N_{tot}) and total volume of the particles (V_{tot}), the time series of which are presented in Fig. 5a and b. The trend statistics for N_{tot} and V_{tot} are presented in Table 3. The N_{tot} and V_{tot} were determined by using the combined TDMPS and APS data for particles smaller than 10 µm in diameter. The relative decrease in V_{tot} ($-4 \% \text{ yr}^{-1}$) was rather similar to that of σ_{sca} ($-3 \% \text{ yr}^{-1}$). Also, Pandolfi et al. (2018) showed a statistically significant trend for σ_{sca} ($-0.588 \text{ Mm}^{-1} \text{ yr}^{-1}$) measured at SMEAR II. They reported negative trends at other European sites as well

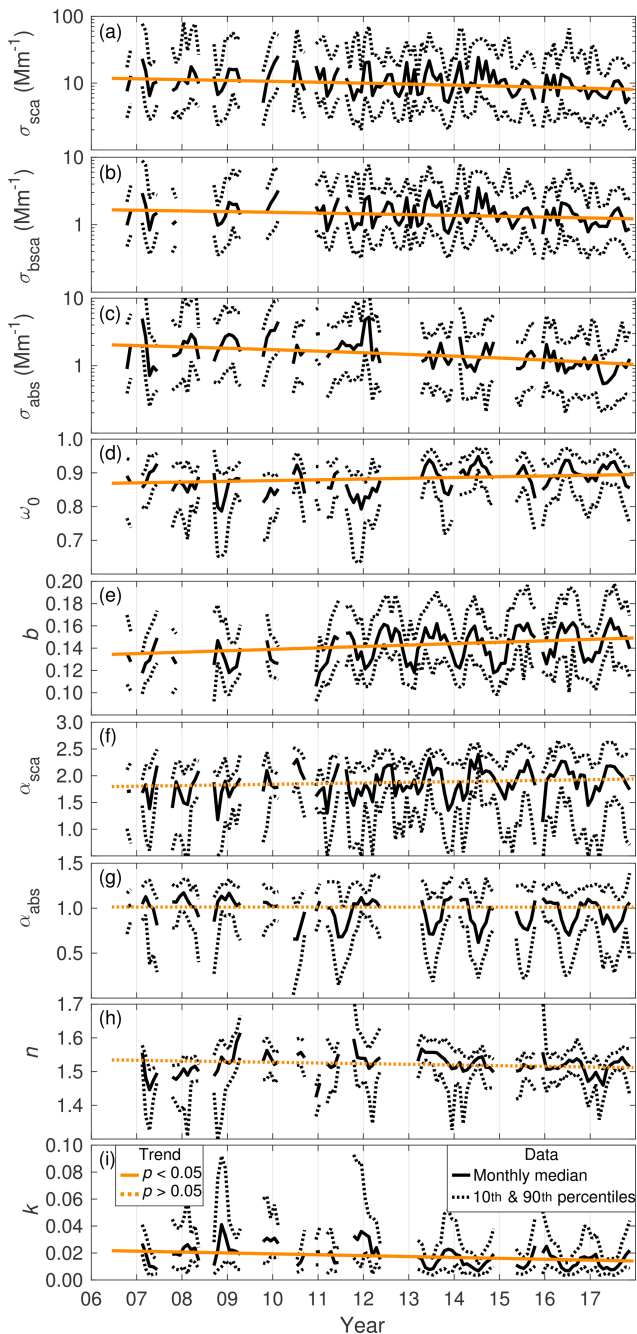


Figure 4. Time series of the PM₁₀ AOPs. The uniform black line presents the monthly median and the dotted black lines present the monthly 10th and 90th percentiles. The trends (see Table 3) of the AOPs are shown with orange lines. If the trend was statistically significant, the line is uniform and if the p value of the trend was > 0.05 , the line is dashed.

and they determined that the average decrease was about -35% for a 10-year period, which is a bit larger reduction than that observed at SMEAR II (-30% for a 10-year period). The results are in line with the decrease in particle number concentrations observed in European countries

Table 3. Slopes of the trends (in absolute values and in estimated percentages per year) and their statistical significance. The lower and upper limits in the 95 % confidence interval for different optical properties are also shown. The trend in the percentage was determined by comparing the slope of the trend with the overall median of the data.

λ (nm)	PM ₁₀				p value	PM ₁					
	Trend (yr ⁻¹)	Lower (yr ⁻¹)	Upper (yr ⁻¹)	p value		Trend (yr ⁻¹)	Lower (yr ⁻¹)	Upper (yr ⁻¹)	p value		
σ_{sca} (Mm ⁻¹)	550	-0.32	-3 %	-0.52	-0.17	<0.01	-0.30	-4 %	-0.55	-0.12	<0.01
σ_{bsca} (Mm ⁻¹)	550	-0.038	-3 %	-0.070	-0.021	<0.01	-0.051	-5 %	-0.087	-0.013	<0.01
σ_{abs} (Mm ⁻¹)	520	-0.086	-6 %	-0.133	-0.044	<0.01	-0.141	-12 %	-0.166	-0.098	<0.01
ω_0	550	2.2e-3	0.3 %	0.7e-3	3.6e-3	<0.01	5.5e-3	0.6 %	1.5e-3	10e-3	<0.01
b	550	1.3e-3	0.9 %	0.9e-3	1.7e-3	<0.01	1.5e-3	1 %	0.7e-3	2.6e-3	<0.01
α_{sca}	450/700	0.012	0.7 %	-0.001	0.024	0.07	0.014	0.6 %	0.004	0.024	<0.01
α_{abs}	370/950	-1.5e-4	0 %	-3.0e-3	2.9e-5	0.95	-3.5e-3	-0.3 %	-7.9e-3	13e-3	0.34
n	550	-2.0e-3	-0 %	-3.8e-3	0.6e-3	0.11	-5.7e-3	-0.4 %	-7.5e-3	-2.9e-3	<0.01
k	550	-6.6e-4	-4 %	-9.1e-4	-3.8e-4	<0.01	-1.3e-3	-6 %	-2.0e-3	-0.7e-3	<0.01
RFE _{H&S} (W m ⁻²)	550	-0.30	-1 %	-0.43	-0.20	<0.01					
RFE _S (W m ⁻²)	550	-0.43	-2 %	-0.64	-0.25	<0.01					
RFE _{S,moist} (W m ⁻²)	550	-0.37	-2 %	-0.50	-0.23	<0.01					
N_{tot} (cm ⁻³)	-40	-3 %	-52	-28	<0.01						
V_{tot} (μg cm ⁻³)	-0.093	-4 %	-0.120	-0.064	<0.01						
GMD _{tot} (nm)	-0.092	-0 %	-0.531	0.342	0.63						
VMD _{tot} (nm)	-12	-1 %	-17	-7	<0.01						

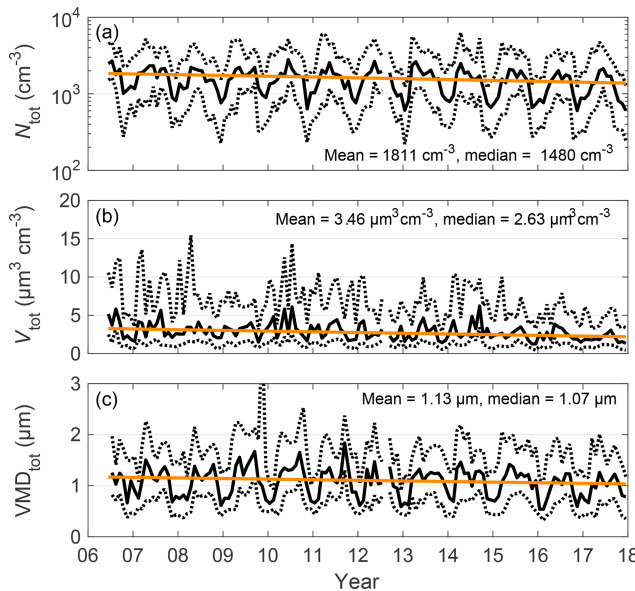


Figure 5. Time series and trends of the total particle ($D_p < 10 \mu\text{m}$) (a) number concentration (N_{tot}), (b) volume (V_{tot}), and (c) VMD_{tot}. The mean and median values of the variables are also marked in the subfigures and the statistics of their slopes are presented in Table 3. The explanations for the different lines are the same as in Fig. 5.

(Asmi et al., 2013). Also, the remotely measured decreasing trend for aerosol optical depth (δ) supports the decreasing trends in Europe (Li et al., 2014). Decreasing trends for σ_{sca} are not only observed in Europe; Collaud Coen et al. (2013) and Sherman et al. (2015) reported negative trends for σ_{sca} in North America as well.

The observed relative decrease in σ_{abs} ($-6 \% \text{ yr}^{-1}$) was about twice as large as that of σ_{sca} ($-3 \% \text{ yr}^{-1}$). The differ-

ences in the trends indicate that during the measurement period, the amount of absorbing material, such as BC and BrC, decreased relatively faster than the amount of scattering material (e.g., sulfate). It is also possible that the decrease in non-absorbing compounds decreased the σ_{abs} since a non-absorbing coating around an absorbing particle can act as a lens, which increases absorption. The study by Collaud Coen et al. (2013), which also included σ_{abs} data, observed negative trends for both σ_{sca} and σ_{abs} at the Bondville measurement station in Illinois, USA, but there the trends of both σ_{sca} and σ_{abs} were about $-3 \% \text{ yr}^{-1}$. Sherman et al. (2015) did not observe this decreasing trend in σ_{abs} later.

Since the aerosol particles were absorbing less light than in the beginning of the measurements, there was a tendency for the ω_0 to increase. As shown by the increase in ω_0 and the decrease in the extensive properties, the air measured at SMEAR II was less polluted than before. Higher ω_0 indicates that the measurements were less affected by particles produced by traffic emissions or incomplete combustion. Li et al. (2014) reported mostly positive trends for ω_0 , which were determined by remote measurements conducted in Europe. The decreasing trend for k supports the tendency for ω_0 to increase since the negative trend for m means that particulate matter absorbs less light. The α_{abs} and n , which are also related to the chemical composition of the particles, showed no significant trends.

The trends of b and α_{sca} describe how the size distribution of the aerosol particles has changed. For the PM₁₀ b and α_{sca} , the trends were positive, but for the α_{sca} however, the p value was 0.07, so there was only weak evidence for the positive trend in α_{sca} . Increasing b indicates that the size distribution moved towards smaller particles. This hypothesis was investigated by conducting the trend analysis for the volumetric and geometric mean diameters of particles smaller

than $10\text{ }\mu\text{m}$ (VMD_{tot} and GMD_{tot}), which were calculated from the size distribution. The results are presented in Table 3. We did not observe a significant trend for the GMD_{tot} , which is sensitive to the smallest particles of the size distribution. However, a statistically significant trend was observed for VMD_{tot} , the time series of which are shown in Fig. 5c. The VMD_{tot} trend statistics are presented in Table 3. The trend for VMD_{tot} depends on the accumulation and coarse-mode particles and therefore correlates better with the extensive AOPs than the GMD (Virkkula et al., 2011). Decreasing VMD_{tot} indicates a shift in the size distribution towards smaller diameters supporting the increasing b and α_{sca} .

In addition to SMEAR II, Pandolfi et al. (2018) observed significant increasing trends for b at several European stations. At SMEAR II they also observed a significant increasing trend for α_{sca} , which was determined by using the wavelength range of 550–700 nm. At other sites, they observed mostly decreasing trends. Pandolfi et al. (2018) suspected that the variation was caused by differing trends of the coarse- and accumulation-mode particle concentrations. Also, Li et al. (2014) observed negative trends for the α_{sca} across Europe and they suggested the trends were caused by a decrease in fine particle emissions.

As a comparison, we also conducted the trend analysis for the PM_1 measurements, even though there were only 7.5-year-long time series available. The trends observed for the PM_1 particles were similar to those of PM_{10} : decreasing trends for the extensive properties and increasing trends for the ω_0 and b . For the PM_1 , the trends for both, b and α_{sca} , were positive and statistically significant. This observation suggests that the concentration of larger particles in the accumulation mode in particular was decreasing since a decrease in coarse particle concentration only could not cause the decreasing trend of $\text{PM}_1 \alpha_{\text{sca}}$ or b . A closer look at the size distribution, which is presented in Sect. S6, pointed out that relatively greatest decrease occurred for accumulation-mode particles that were 500–800 nm in diameter. On average, the volume size distribution of accumulation-mode particles peaks around 300 nm (see Fig. 3) so the greatest decrease occurred at the larger sizes of the accumulation mode.

The decrease in the larger size of the accumulation mode might be caused by a decrease in long-range-transported pollution. Aged pollution particles might be grown by other substances, such as SO_2 in the atmosphere, so their sizes are larger than freshly emitted or formed particles. SO_2 emissions have decreased in Europe (Tørseth et al., 2012), which supports this assumption. A trajectory analysis by Virkkula et al. (2011) showed that α_{sca} was clearly higher in air masses from continental Europe than from the North Atlantic but also that the highest α_{sca} values were measured in air mass sources from within southern Finland, which would suggest that larger particles are not from near the station.

The installation of the Nafion dryers in 2010 could have caused an artificial decrease in the AOPs since the dryers increase the deposition of the particles and may decrease the

sizes of hygroscopic particles. However, the similar trend between the PM_1 and PM_{10} AOPs does not support this suspicion since during the PM_1 measurements, there were no large changes in the measurement line, so the observed trends were probably not caused by any technical issues in the measurement line.

In addition to the general trends, we also investigated how the trends of σ_{sca} and σ_{abs} varied between the seasons. In this analysis, the periods of $\text{RH} > 40\%$ were included in order to avoid the data gaps in summer and autumn before 2010 and to have time series with equal lengths for each season. The moist σ_{sca} was estimated to dry conditions according to Eqs. (1) and (2). The trends were determined separately for spring (March, April, May), summer (June, July, August), autumn (September, October, November), and winter (December, January, February). The trend calculations were conducted by using the monthly medians (see time series in Fig. S3) and the results are presented in Table 4.

Table 4 shows that σ_{sca} and σ_{abs} had a decreasing trend for each season, but in the autumn the trends were not significant. Both σ_{sca} and σ_{abs} experience the fastest absolute decrease in winter when the energy consumption is the highest and pollution sources are more pronounced; conversely, the trends were the least negative in summer when there is less pollution. In spring, the absolute trends were less negative than compared to winter.

3.3 Seasonality and long-term trend of radiative forcing efficiency

To study the climate impact of the aerosol particles, the aerosol radiative forcing efficiency (RFE) and the average values, trends, and seasonal variations were investigated. We determined three different kind of RFE: (1) $\text{RFE}_{\text{H}\&\text{S}}$ was calculated to dry aerosol particles by using global average values suggested by Haywood and Shine (1995), (2) RFE_{S} was also calculated to dry aerosols but here we used more realistic environmental parameters (D , R_{S} , and A_{C}) at SMEAR II and here the seasonality of the parameters was also taken into account, and (3) $\text{RFE}_{\text{S},\text{moist}}$ also used the more realistic and seasonally varying environmental parameters but here we took into account the effect of ambient RH on ω_0 and b . The statistics of the $\text{RFE}_{\text{H}\&\text{S}}$, RFE_{S} , and $\text{RFE}_{\text{S},\text{moist}}$ are presented in Table 1 and their time series and seasonal variations are presented in Fig. 6.

In general, the aerosols measured at SMEAR II tended to have a cooling effect on the climate ($\text{RFE} < 0$) as seen in Table 1. By using the global average values suggested by Haywood and Shine (1995), the mean value of $\text{RFE}_{\text{H}\&\text{S}}$ was -22 W m^{-2} . This was about 12 % less negative than the mean value of $\text{RFE}_{\text{H}\&\text{S}}$ (about -25 W m^{-2}) determined by Sherman et al. (2015) for different North American stations. The difference is explained by a higher mean value of ω_0 (about 0.91) observed by Sherman et al. (2015). The mean value of b (about 0.14) was similar if compared to

Table 4. Slopes of the seasonal trends and their statistical significance for σ_{sca} and σ_{abs} . The trend in the percentage was determined by comparing the slope of the trend with the seasonal median of the data.

	$\sigma_{\text{sca}} (\text{Mm}^{-1})$				$\sigma_{\text{abs}} (\text{Mm}^{-1})$				
	Trend (yr^{-1})	Lower (yr^{-1})	Upper (yr^{-1})	p value	Trend (yr^{-1})	Lower (yr^{-1})	Upper (yr^{-1})	p value	
Spring	-0.44	-5 %	-0.84	-0.04	< 0.05	-0.12	-9 %	-0.20	-0.05 < 0.01
Summer	-0.38	-3 %	-0.79	-0.14	< 0.01	-0.06	-5 %	-0.11	-0.03 < 0.01
Autumn	-0.12	-1 %	-0.49	0.17	0.48	-0.04	-3 %	-0.10	0.03 0.14
Winter	-0.85	-7 %	-1.60	-0.20	< 0.01	-0.17	-8 %	-0.31	-0.03 < 0.05

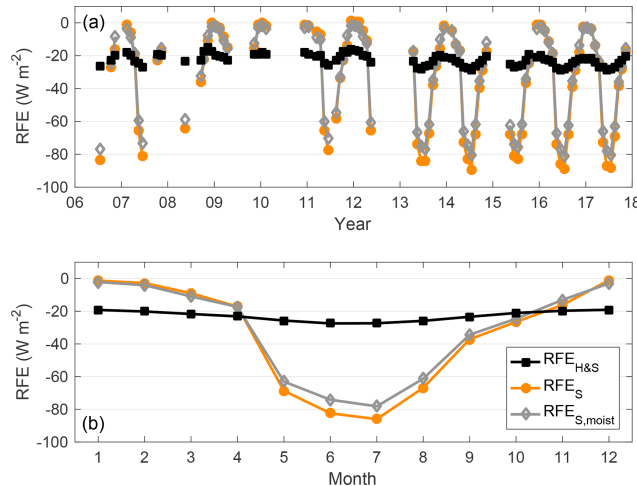


Figure 6. Variations in the different radiative forcing efficiencies at SMEAR II in 2006–2018. (a) Time series of the $\text{RFE}_{\text{H}\&\text{S}}$, RFE_S , and $\text{RFE}_{\text{S},\text{moist}}$. The monthly medians are presented if the month had at least 14 d of valid data. (b) Seasonal variation in the $\text{RFE}_{\text{H}\&\text{S}}$, RFE_S , and $\text{RFE}_{\text{S},\text{moist}}$ as overall monthly medians. RFE was calculated for PM_{10} particles.

average values observed at SMEAR II. A mean value of $\text{RFE}_{\text{H}\&\text{S}} = 25 \text{ W m}^{-2}$ was also determined at SORPES station in Nanjing, China (Shen et al., 2018). Shen et al. (2018) observed a lower mean value of b (0.12 at 520 nm), which would increase the $\text{RFE}_{\text{H}\&\text{S}}$. However, they also observed a notably higher mean value of ω_0 (0.93 at 520 nm) at SORPES and that overcame the effect of the lower parameter b .

If the seasonal variation in D , A_C , and R_S were taken into account, the RFE became more negative at SMEAR II. The median value of RFE_S , which takes the seasonality of the environmental parameters into account, was -26 W m^{-2} , lower than the median value of $\text{RFE}_{\text{H}\&\text{S}}$, which was -23 W m^{-2} . This was mainly due to the higher D and lower R_S and A_C in summer. If the ambient RH was taken into account, the median value for the $\text{RFE}_{\text{S},\text{moist}}$ (-24 W m^{-2}) increased a bit compared to RFE_S . Taking the ambient RH (that was $\text{RH} > 40\%$ every month) into account increases the ω_0 due to increase in the scattering. At the same time the b decreases since the particles grow in size and scatter relatively less

light backwards (Birmili et al., 2009). These two changes have opposite effects on the RFE: increasing ω_0 decreases the RFE, and decreasing b increases the RFE. Here the decreasing b overcomes the effect of ω_0 and therefore the median $\text{RFE}_{\text{S},\text{moist}}$ is higher than that of RFE_S .

The long-term trends of ω_0 and b tended to increase, which makes the $\text{RFE}_{\text{H}\&\text{S}}$ decrease (i.e., become more negative). The decreasing $\text{RFE}_{\text{H}\&\text{S}}$ means that the properties of dry aerosol particles have changed so that they cool the climate more efficiently. The trends for the $\text{RFE}_{\text{H}\&\text{S}}$, RFE_S , and $\text{RFE}_{\text{S},\text{moist}}$ are presented in Table 3 as well. Since we used seasonal averages in calculating the RFE_S and $\text{RFE}_{\text{S},\text{moist}}$, their trends were also dependent only on the changes of the ω_0 and b and thus their trends of RFE_S and $\text{RFE}_{\text{S},\text{moist}}$ also decrease and are similar in magnitude to the trend for $\text{RFE}_{\text{H}\&\text{S}}$. However, in reality the trend of RFE_S and $\text{RFE}_{\text{S},\text{moist}}$, which take into account the realistic environmental parameters, do not depend only on the ω_0 and b . For example, a decrease in the snow cover due to global warming would decrease the R_S and make the decrease in RFE_S and $\text{RFE}_{\text{S},\text{moist}}$ steeper. Here, we omitted further analysis on the effect that the changes of A_C , R_S , T_{at} , and RH have on the RFE_S and $\text{RFE}_{\text{S},\text{moist}}$.

The seasonal variation in the $\text{RFE}_{\text{H}\&\text{S}}$ followed the seasonal cycles of the ω_0 and b . The $\text{RFE}_{\text{H}\&\text{S}}$ was minimal in summer and maximal in winter. Since b was lowest (forward-scattering particles) and the ω_0 is also low (absorbing particles) in winter, the particles clearly did not have as strong a cooling effect as in summer when particles were smaller and highly scattering. If the seasonal changes of D , A_C , and R_S were taken into account, the seasonal variability of RFEs was amplified remarkably as seen in Fig. 6b. In winter, the higher R_S causes the aerosol particles to be less cooling or even warming, but since the D is low and the A_C high (see Fig. S1), the aerosol particles have less of an effect (RFE closer to zero) than in summer. We chose to use the R_S determined for a boreal forest according to the surroundings of SMEAR II. However, the area around the station also consists of fields and lakes, which in winter would act as smooth snow fields. Even for snow containing impurities the R_S is notably higher (> 0.7) than R_S for snow-covered boreal forest (Warren and Wiscombe, 1980). Using $R_S = 0.7$ for winter-

time data would increase the RFE_S and amplify its seasonal variation even more.

Taking the effect of ambient RH into account decreases the seasonality in RFE_S a bit. The seasonality of RH is presented in Fig. S1d and on average the RH is higher in winter than in summer. Figure 6b shows that compared to RFE_S, the RFE_{S,moist} is less negative in summer when the effect of RH on b overcomes the effect on ω_0 . Also, Fierz-Schmidhauser et al. (2010) observed this kind of behavior at the Jungfraujoch station. In winter, the situation was actually the opposite and the RFE_{S,moist} was more negative than RFE_S. However the difference were small, partly due to the low D and high A_C . In general, the effect of the RH on the seasonal variation in RFE was smaller than the effect of taking the seasonal variation in D , A_C , and R_S into account.

The RFE (or $\Delta F \delta^{-1}$) describes only the efficiency of the aerosol particles in cooling or warming the climate per unit of aerosol optical depth (δ). Even if the RFE was very negative, the influence of aerosol particles on the climate would be small if the δ was small. Equation (13) assumes that the properties of aerosol particles are uniform in the atmospheric column, which is rarely the case in reality. In ambient air, we should also take into account the variability in RH as a function of height, since at the top of the boundary layer we typically have RH values close to 100 %. Here, we determined the RFE by using the RH measured near the ground (16 m). The simplified RFE does not give an absolute value for the aerosol forcing; however, it can still indicate how the changes in AOPs affect the climate.

3.4 Effect of excluding the moist data

Only about 62 % of AOP data measured before 2010 were marked as valid. A big fraction of the not-valid data were invalidated due to too high RH. If we take the moist data into account and estimated it to dry conditions, the data coverage from June 2006 to December 2010 increases to 87 %. To test, if excluding large numbers of data that had a significant difference to the results, we used Eqs. (1) and (2) to estimate the moist (RH > 40 %) σ_{sca} and σ_{bsca} to dry conditions and included these data in calculating the median values and in the trend analysis. Also, moist (RH > 40 %) σ_{abs} measurements were included here.

If the moist periods of σ_{sca} and σ_{abs} measurements were included in the analysis and the moist scattering data were estimated to dry conditions by using the parametrization suggested by Andrews et al. (2006), we would get median values of $\sigma_{\text{sca}} = 10.4 \text{ Mm}^{-1}$, $\sigma_{\text{bsca}} = 1.5 \text{ Mm}^{-1}$, $\sigma_{\text{abs}} = 1.5 \text{ Mm}^{-1}$, $\omega_0 = 0.88$, $b = 0.14$, $\alpha_{\text{abs}} = 0.97$, and $\text{RFE}_{\text{H\&S}} = -23 \text{ W m}^{-2}$ for PM₁₀ (σ_{sca} , σ_{bsca} , ω_0 , b , and $\text{RFE}_{\text{H\&S}}$ at 550 nm, σ_{abs} at 520 nm, α_{abs} at 370 nm/950). Taking the moist samples into account, the σ_{sca} and σ_{abs} increased in summer and autumn (see Fig. S6). We could not determine the α_{sca} since we only converted the σ_{sca} at 550 nm to dry conditions. If we used the parameters observed by

Zieger et al. (2015), the median $\sigma_{\text{sca}} = 10.3 \text{ Mm}^{-1}$, which is very close to the value obtained by using the parameters suggested by Andrews et al. (2006). For the extensive properties, also including the moist data increased their median values by about 7 % and for the intensive properties there was no notable effect. Omitting the moist data periods from the data set does not seem to have a large effect on the median AOPs in this data set.

Including the originally omitted data in the trend analysis, we observed statistically significant (p value < 0.05) trends for the PM₁₀ σ_{sca} , σ_{bsca} , σ_{abs} , ω_0 , and RFE with the slopes of $-4 \% \text{ yr}^{-1}$, $-5 \% \text{ yr}^{-1}$, $-5 \% \text{ yr}^{-1}$, $0.2 \% \text{ yr}^{-1}$, and $0.6 \% \text{ yr}^{-1}$, respectively. Still, there were decreasing trends for extensive properties and positive trends for ω_0 . For b , there was no significant trend anymore due to the difference between the σ_{sca} and σ_{bsca} trends decreasing from $3 \% \text{ yr}^{-1}$ to $1 \% \text{ yr}^{-1}$ if compared against the trends that were determined only for the dry conditions. Including the moist data and acquiring longer data sets in the trend analysis suggests that the relative difference between the trends of σ_{sca} and σ_{abs} might not be that large.

4 Summary and conclusions

In this study, we presented 11.5-year-long time series of AOPs measured at SMEAR II, a station in southern Finland. Compared to regional and rural European sites, the σ_{sca} at the boreal SMEAR II station was low. However, the average σ_{sca} and σ_{abs} were higher than those observed at other Finnish measurement stations that were the arctic station in Pallas and the semi-urban station in Kuopio, eastern Finland. Because of the more southern location, SMEAR II was probably more affected by regional emissions and long-transport pollution from Europe than the other Finnish measurement sites, which would explain the higher concentrations.

The highest σ_{sca} and σ_{abs} were measured in winter when the boundary layer is lower and the pollution is not diluted as efficiently as in summer. Transported pollution from the regional area and from Europe also increases the concentration in winter, when the energy consumption is higher. In winter, the ω_0 was low (i.e., absorption was relatively high compared to scattering), which also indicates that there was a higher fraction of particles from anthropogenic combustion sources. The σ_{sca} also had high values in summer but the σ_{abs} had its minimum and therefore the ω_0 reached its maximum in summer. This observation indicates that the particle concentration was high in summer due to active vegetation.

Closer investigation on the size distribution revealed that the seasonal variations in b and α_{sca} were caused by shifting accumulation mode and not by changes in the coarse-mode particle concentration. In summer, b and α_{sca} had their maxima (i.e., there was a higher fraction of smaller accumulation-mode particles) and in winter they had their minima (i.e.,

there was a higher fraction of large accumulation-mode particles).

The extensive AOPs, as well as the aerosol number and volume concentrations, tended to decrease. Our observations were in line with other studies conducted in Europe and North America, which also observed decreasing trends for the extensive AOPs (Collaud Coen et al., 2013; Pandolfi et al., 2018; Sherman et al., 2015), number concentration (Asmi et al., 2013), and aerosol optical depth (Li et al., 2014). This uniform decreasing trend in the number of aerosol particles suggests that the anthropogenic emissions have been decreasing in Europe and North America. The observed tendency for b and α_{sca} to increase together with the decreasing extensive properties indicated that the particle size distribution consisted of fewer larger particles. A more detailed investigation revealed that the number of larger accumulation-mode particles (500–800 nm in diameter) decreased relatively the fastest, which would indicate a decrease in transported anthropogenic pollution.

Since the aerosol particles were scattering light more efficiently back to the hemisphere and because they absorbed less light than in the beginning of the measurements, their RFE tended to decrease (i.e., became more negative), which means that the ability of aerosols to cool the climate per unit δ increased. However, since the extensive properties and particle number concentration were decreasing, which means that the δ decreased as well, the total aerosol forcing was probably also decreasing. Here, we only studied the effect of AOPs on the RFE. Studying and also taking the long-term trends of the environmental parameters into account would give a more realistic trend for the RFE.

Data availability. All the data presented in this study are open access. The optical properties and the size distribution data from SMEAR II have been uploaded on the EBAS database (NILU, 2019: <http://ebas.nilu.no/>) run by the Norwegian Institute for Air Research (NILU). Meteorological parameters measured at SMEAR II, such as the RH used here, can be accessed by the Smart-SMEAR online tool (<https://avaa.tdata.fi/web/smart>, last access: 18 March 2019, Junninen et al., 2009). Also, the Finnish Meteorological Institute provides open-access data and we used their online data tool (FMI, 2019: <https://ilmatieteenlaitos.fi/havaintojen-lataus>) to access the ceilometer data measured at Halli airport.

Supplement. The supplement related to this article is available online at: <https://doi.org/10.5194/acp-19-11363-2019-supplement>.

Author contributions. KL performed the data analysis and wrote the paper together with AV. PA and AV have set up the long-term measurements of AOPs at SMEAR II. All authors reviewed and commented on the paper.

Acknowledgements. We thank Andreas Petzold and the two anonymous referees, whose reviews and suggestions helped us to improve the paper.

Financial support. This research has been supported by the Academy of Finland (grant no. 307331), the European Union Seventh Framework Programme ACTRIS (grant no. 262254), and the European Union's Horizon 2020 Research and Innovation program via projects ACTRIS-2 (grant no. 654109) and iCUPE (grant no. 689443).

Review statement. This paper was edited by Andreas Petzold and reviewed by two anonymous referees.

References

- Aalto, P., Hämeri, K., Becker, E., Weber, R., Salm, J., Mäkelä, J. M., Hoell, C., O'dowd, C. D., Hansson, H.-C., Väkevä, M., Koponen, I. K., Buzorius, G., and Kulmala, M.: Physical characterization of aerosol particles during nucleation events, *Tellus B*, 53, 344–358, 2001.
- Anderson, T. L. and Ogren, J. A.: Determining aerosol radiative properties using the TSI 3563 integrating nephelometer, *Aerosol Sci. Tech.*, 29, 57–69, 1998.
- Andrews, E., Sheridan, P. J., Fiebig, M., McComiskey, A., Ogren, J. A., Arnott, P., Covert, D., Elleman, R., Gasparini, R., Collins, D., Jonsson, H., Schmid, B., and Wang, J.: Comparison of methods for deriving aerosol asymmetry parameter, *J. Geophys. Res.-Atmos.*, 111, D05S04, <https://doi.org/10.1029/2004JD005734>, 2006.
- Andrews, E., Ogren, J. A., Bonasoni, P., Marinoni, A., Cuevas, E., Rodriguez, S., Sun, J. Y., Jaffe, D. A., Fischer, E. V., Baltensperger, U., Weingartner, E., Collaud Coen, M., Sharma, S., Macdonald, A. M., Leaitch, W. R., Lin, N.-H., Laj, P., Arsov, T., Kalapov, I., Jefferson, A., and Sheridan, P. J.: Climatology of aerosol radiative properties in the free troposphere, *Atmos. Res.*, 102, 365–393, 2011.
- Andrews, E., Sheridan, P.J., Ogren, J.A., Hageman, D., Jefferson, A., Wendell, J., Alástuey, A., Alados-Arboledas, L., Bergin, M., Ealo, M., Hallar, A.G., Hoffer, A., Kalapov, I., Keywood, M., Kim, J., Kim, S.W., Kolonjari, F., Labuschagne, C., Lin, N.H., Macdonald, A., Mayol-Bracero, O.L., McCubbin, I.B., Pandolfi, M., Reisen, F., Sharma, S., Sherman, J.P., Sorribas, M. and Sun, J.: Overview of the NOAA/ESRL federated aerosol network, *B. Am. Meteorol. Soc.*, 100, 123–135, 2019.
- Ångström, A.: On the atmospheric transmission of sun radiation and on dust in the air, *Geogr. Ann.*, 11, 156–166, 1929.
- Arnott, W. P., Hamasha, K., Moosmüller, H., Sheridan, P. J., and Ogren, J. A.: Towards aerosol light-absorption measurements with a 7-wavelength aethalometer: Evaluation with a photoacoustic instrument and 3-wavelength nephelometer, *Aerosol Sci. Tech.*, 39, 17–29, 2005.
- Asmi, A., Collaud Coen, M., Ogren, J. A., Andrews, E., Sheridan, P., Jefferson, A., Weingartner, E., Baltensperger, U., Bukowiecki, N., Lihavainen, H., Kivekäs, N., Asmi, E., Aalto, P. P., Kulmala, M., Wiedensohler, A., Birmili, W., Hamed, A., O'Dowd, C., G

- Jennings, S., Weller, R., Flentje, H., Fjaeraa, A. M., Fiebig, M., Myhre, C. L., Hallar, A. G., Swietlicki, E., Kristensson, A., and Laj, P.: Aerosol decadal trends – Part 2: In-situ aerosol particle number concentrations at GAW and ACTRIS stations, *Atmos. Chem. Phys.*, 13, 895–916, <https://doi.org/10.5194/acp-13-895-2013>, 2013.
- Backman, J., Schmeisser, L., Virkkula, A., Ogren, J. A., Asmi, E., Starkweather, S., Sharma, S., Eleftheriadis, K., Uttal, T., Jefferson, A., Bergin, M., Makshtas, A., Tunved, P., and Fiebig, M.: On Aethalometer measurement uncertainties and an instrument correction factor for the Arctic, *Atmos. Meas. Tech.*, 10, 5039–5062, <https://doi.org/10.5194/amt-10-5039-2017>, 2017.
- Bergin, M. H., Ogren, J. A., Schwartz, S. E., and McInnes, L. M.: Evaporation of ammonium nitrate aerosol in a heated nephelometer: Implications for field measurements, *Environ. Sci. Technol.*, 31, 2878–2883, 1997.
- Birmili, W., Schwirn, K., Nowak, A., Petäjä, T., Joutsensaari, J., Rose, D., Wiedensohler, A., Hämeri, K., Aalto, P., Kulmala, M., and Boy, M.: Measurements of humidified particle number size distributions in a Finnish boreal forest: derivation of hygroscopic particle growth factors, *Boreal Environ. Res.*, 14, 458–480, 2009.
- Carrico, C. M., Kus, P., Rood, M. J., Quinn, P. K., and Bates, T. S.: Mixtures of pollution, dust, sea salt, and volcanic aerosol during ACE-Asia: Radiative properties as a function of relative humidity, *J. Geophys. Res.-Atmos.*, 108, 8650, <https://doi.org/10.1029/2003JD003405>, 2003.
- Charlson, R. J., Schwartz, S., Hales, J., Cess, R. D., Coakley, J. J., Hansen, J., and Hofmann, D.: Climate forcing by anthropogenic aerosols, *Science*, 255, 423–430, 1992.
- Collaud Coen, M., Weingartner, E., Nyeki, S., Cozic, J., Henning, S., Verheggen, B., Gehrig, R., and Baltensperger, U.: Long-term trend analysis of aerosol variables at the high-alpine site Jungfraujoch, *J. Geophys. Res.-Atmos.*, 112, D13213, <https://doi.org/10.1029/2006JD007995>, 2007.
- Collaud Coen, M., Weingartner, E., Apituley, A., Ceburnis, D., Fierz-Schmidhauser, R., Flentje, H., Henzing, J. S., Jennings, S. G., Moerman, M., Petzold, A., Schmid, O., and Baltensperger, U.: Minimizing light absorption measurement artifacts of the Aethalometer: evaluation of five correction algorithms, *Atmos. Meas. Tech.*, 3, 457–474, <https://doi.org/10.5194/amt-3-457-2010>, 2010.
- Collaud Coen, M., Andrews, E., Asmi, A., Baltensperger, U., Bukowiecki, N., Day, D., Fiebig, M., Fjaeraa, A. M., Flentje, H., Hyvärinen, A., Jefferson, A., Jennings, S. G., Kouvarakis, G., Lihavainen, H., Lund Myhre, C., Malm, W. C., Mihapopoulos, N., Molenar, J. V., O'Dowd, C., Ogren, J. A., Schichtel, B. A., Sheridan, P., Virkkula, A., Weingartner, E., Weller, R., and Laj, P.: Aerosol decadal trends – Part 1: In-situ optical measurements at GAW and IMPROVE stations, *Atmos. Chem. Phys.*, 13, 869–894, <https://doi.org/10.5194/acp-13-869-2013>, 2013.
- Delene, D. J. and Ogren, J. A.: Variability of aerosol optical properties at four North American surface monitoring sites, *J. Atmos. Sci.*, 59, 1135–1150, 2002.
- NILU: EBAS database, Norwegian Institute for Air Research, available at: <http://ebas.nilu.no/>, last access: 18 March 2019.
- Ehn, M., Thornton, J., Kleist, E., Sipila, M., Junninen, H., Pullinen, I., Springer, M., Rubach, F., Tillmann, R., Lee, B., Lopez-Hilfiker, F., Andres, S., Acir, I., Rissanen, M., Jokinen, T., Schobesberger, S., Kangasluoma, J., Kontkanen, J., Nieminen, T., Kurten, T., Nielsen, L., Jorgensen, S., Kjaergaard, H., Canagaratna, M., Dal Maso, M., Berndt, T., Petaja, T., Wahner, A., Kerminen, V., Kulmala, M., Worsnop, D., Wildt, J., and Mentel, T.: A large source of low-volatility secondary organic aerosol, *Nature*, 506, 476–479, <https://doi.org/10.1038/nature13032>, 2014.
- Fierz-Schmidhauser, R., Zieger, P., Gysel, M., Kammermann, L., DeCarlo, P. F., Baltensperger, U., and Weingartner, E.: Measured and predicted aerosol light scattering enhancement factors at the high alpine site Jungfraujoch, *Atmos. Chem. Phys.*, 10, 2319–2333, <https://doi.org/10.5194/acp-10-2319-2010>, 2010.
- FMI: Havaintojen lataus, available at: <https://ilmatieteenlaitos.fi/havaintojen-lataus>, last access: 18 March 2019 (in Finnish).
- Gilbert, R. O.: Statistical methods for environmental pollution monitoring, John Wiley & Sons, New York, 1987.
- Gyawali, M., Arnott, W. P., Lewis, K., and Moosmüller, H.: In situ aerosol optics in Reno, NV, USA during and after the summer 2008 California wildfires and the influence of absorbing and non-absorbing organic coatings on spectral light absorption, *Atmos. Chem. Phys.*, 9, 8007–8015, <https://doi.org/10.5194/acp-9-8007-2009>, 2009.
- Hari, P. and Kulmala, M.: Station for Measuring Ecosystem–Atmosphere Relations, *Boreal Environ. Res.*, 10, 315–322, 2005.
- Hari, P., Nikinmaa, E., Pohja, T., Siivola, E., Bäck, J., Vesala, T., and Kulmala, M.: Station for measuring ecosystem-atmosphere relations: SMEAR, in: Physical and Physiological Forest Ecology, Springer, 471–487, 2013.
- Haywood, J. and Shine, K.: The effect of anthropogenic sulfate and soot aerosol on the clear sky planetary radiation budget, *Geophys. Res. Lett.*, 22, 603–606, 1995.
- Hienola, A. I., Pietikäinen, J.-P., Jacob, D., Pozdun, R., Petäjä, T., Hyvärinen, A.-P., Sogacheva, L., Kerminen, V.-M., Kulmala, M., and Laaksonen, A.: Black carbon concentration and deposition estimations in Finland by the regional aerosol-climate model REMO-HAM, *Atmos. Chem. Phys.*, 13, 4033–4055, <https://doi.org/10.5194/acp-13-4033-2013>, 2013.
- Hyvärinen, A.-P., Kolmonen, P., Kerminen, V.-M., Virkkula, A., Leiskinen, A., Komppula, M., Hatakka, J., Burkhardt, J., Stohl, A., Aalto, P., Kulmala, M., Lehtinen, K. E. J., Viisanen, Y., and Lihavainen, H.: Aerosol black carbon at five background measurement sites over Finland, a gateway to the Arctic, *Atmos. Environ.*, 45, 4042–4050, 2011.
- Junninen, H., Lauri, A., Keronen, P., Aalto, P., Hiltunen, V., Hari, P., and Kulmala, M.: Smart-SMEAR: on-line data exploration and visualization tool for SMEAR stations, *Boreal Environ. Res.*, 14, 447–457, 2009.
- Karvosenoja, N., Kangas, L., Kupiainen, K., Kukkonen, J., Karppinen, A., Sofiev, M., Tainio, M., Paunu, V.-V., Ahtoniemi, P., Tuomisto, J. T., and Porvari, P.: Integrated modeling assessments of the population exposure in Finland to primary PM_{2.5} from traffic and domestic wood combustion on the resolutions of 1 and 10 km, *Air Qual. Atmos. Hlth.*, 4, 179–188, 2011.
- Kulmala, M., Vehkamäki, H., Petäjä, T., Dal Maso, M., Lauri, A., Kerminen, V.-M., Birmili, W., and McMurry, P.: Formation and growth rates of ultrafine atmospheric particles: a review of observations, *J. Aerosol Sci.*, 35, 143–176, 2004.
- Kulmala, M., Kontkanen, J., Junninen, H., Lehtipalo, K., Manninen, H. E., Nieminen, T., Petäjä, T., Sipilä, M., Schobesberger, S., Rantala, P., Franchin, A., Jokinen, T., Järvinen, E., Äijälä, M.,

- Kangasluoma, J., Hakala, J., Aalto, P. P., Paasonen, P., Mikkilä, J., Vanhanen, J., Aalto, J., Hakola, H., Makkonen, U., Ruuskanen, T., Mauldin, R. L., Duplissy, J., Vehkämäki, H., Bäck, J., Kortelainen, A., Riipinen, I., Kurtén, T., Johnston, M. V., Smith, J. N., Ehn, M., Mentel, T. F., Lehtinen, K. E. J., Laaksonen, A., Kerminen, V.-M., and Worsnop, D. R.: Direct observations of atmospheric aerosol nucleation, *Science*, 339, 943–946, 2013.
- Kuusinen, N., Kolari, P., Levula, J., Porcar-Castell, A., Stenberg, P., and Berninger, F.: Seasonal variation in boreal pine forest albedo and effects of canopy snow on forest reflectance, *Agr. Forest Meteorol.*, 164, 53–60, 2012.
- Lack, D. A. and Cappa, C. D.: Impact of brown and clear carbon on light absorption enhancement, single scatter albedo and absorption wavelength dependence of black carbon, *Atmos. Chem. Phys.*, 10, 4207–4220, <https://doi.org/10.5194/acp-10-4207-2010>, 2010.
- Laj, P., Klausen, J., Bilde, M., Plass-Duelmer, C., Pappalardo, G., Clerbaux, C., Baltensperger, U., Hjorth, J., Simpson, D., Reimann, S., Coheur, P. F., Richter, A., de Maziére, M., Rudich, Y., McFiggans, G., Tørseth, K., Wiedensohler, A., Morin, S., Schulz, M., Allan, J., Attié, J. L., Barnes, I., Birmilli, W., Cammas, P., Dommen, J., Dorn, H. P., Fuzzi, J. S., Glasius, M., Hermann, M., Kinne, S., Koren, I., Madonna, F., Maione, M., Massling, A., Moehler, O., Mona, L., Müller, D., Müller, T., Orphal, J., Peuch, W. H., Stratmann, F., Tanré, D., Tyndall, D., Riziq, A. A., Van Roozendael, M., Villani, P., Weiner, B., Wex, H., and Zardini, A.: Measuring atmospheric composition change, *Atmos. Environ.*, 43, 5351–5414, 2009.
- Leskinen, A., Arola, A., Komppula, M., Portin, H., Tiitta, P., Miettinen, P., Romakkaniemi, S., Laaksonen, A., and Lehtinen, K. E. J.: Seasonal cycle and source analyses of aerosol optical properties in a semi-urban environment at Puijo station in Eastern Finland, *Atmos. Chem. Phys.*, 12, 5647–5659, <https://doi.org/10.5194/acp-12-5647-2012>, 2012.
- Li, J., Carlson, B. E., Dubovik, O., and Lacis, A. A.: Recent trends in aerosol optical properties derived from AERONET measurements, *Atmos. Chem. Phys.*, 14, 12271–12289, <https://doi.org/10.5194/acp-14-12271-2014>, 2014.
- Lihavainen, H., Hyvärinen, A., Asmi, E., Hatakka, J., and Viisanen, Y.: Long-term variability of aerosol optical properties in northern Finland, *Boreal Environ. Res.*, 20, 526–541, 2015.
- Lohmann, U. and Feichter, J.: Global indirect aerosol effects: a review, *Atmos. Chem. Phys.*, 5, 715–737, <https://doi.org/10.5194/acp-5-715-2005>, 2005.
- Müller, T., Henzing, J. S., de Leeuw, G., Wiedensohler, A., Alastuey, A., Angelov, H., Bizjak, M., Collaud Coen, M., Engström, J. E., Gruening, C., Hillamo, R., Hoffer, A., Imre, K., Ivanow, P., Jennings, G., Sun, J. Y., Kalivitis, N., Karlsson, H., Komppula, M., Laj, P., Li, S.-M., Lunder, C., Marinoni, A., Martins dos Santos, S., Moerman, M., Nowak, A., Ogren, J. A., Petzold, A., Pichon, J. M., Rodriguez, S., Sharma, S., Sheridan, P. J., Teinilä, K., Tuch, T., Viana, M., Virkkula, A., Weingartner, E., Wilhelm, R., and Wang, Y. Q.: Characterization and intercomparison of aerosol absorption photometers: result of two intercomparison workshops, *Atmos. Meas. Tech.*, 4, 245–268, <https://doi.org/10.5194/amt-4-245-2011>, 2011.
- Mätzler, C.: MATLAB functions for Mie scattering and absorption, version 2, Institut für Angewandte Physik, University of Bern, Bern, 2002.
- Nessler, R., Weingartner, E., and Baltensperger, U.: Effect of humidity on aerosol light absorption and its implications for extinction and the single scattering albedo illustrated for a site in the lower free troposphere, *J. Aerosol Sci.*, 36, 958–972, 2005.
- Ogren, J. A.: A systematic approach to in situ observations of aerosol properties, in: *Aerosol Forcing of Climate*, edited by: Charlson, R. J. and Heintzenberg, J., John Wiley & Sons, New York, 215–226, 1995.
- Pandolfi, M., Alados-Arboledas, L., Alastuey, A., Andrade, M., Angelov, C., Artiñano, B., Backman, J., Baltensperger, U., Bonasoni, P., Bukowiecki, N., Collaud Coen, M., Conil, S., Coz, E., Crenn, V., Dudoit, V., Ealo, M., Eleftheriadis, K., Favez, O., Fetfatzis, P., Fiebig, M., Flentje, H., Ginot, P., Gysel, M., Henzing, B., Hoffer, A., Holubova Smejkalova, A., Kalapov, I., Kalivitis, N., Kouvarakis, G., Kristensson, A., Kulmala, M., Lihavainen, H., Lunder, C., Luoma, K., Lyamani, H., Marinoni, A., Mihalopoulos, N., Moerman, M., Nicolas, J., O'Dowd, C., Petäjä, T., Petit, J.-E., Pichon, J. M., Prokopiuk, N., Putaud, J.-P., Rodríguez, S., Sciare, J., Sellegri, K., Swietlicki, E., Titos, G., Tuch, T., Tunved, P., Ulevicius, V., Vaishya, A., Vana, M., Virkkula, A., Vratolis, S., Weingartner, E., Wiedensohler, A., and Laj, P.: A European aerosol phenomenology – 6: scattering properties of atmospheric aerosol particles from 28 ACTRIS sites, *Atmos. Chem. Phys.*, 18, 7877–7911, <https://doi.org/10.5194/acp-18-7877-2018>, 2018.
- Ramanathan, V., Crutzen, P., Kiehl, J., and Rosenfeld, D.: Aerosols, climate, and the hydrological cycle, *Science*, 294, 2119–2124, 2001.
- Sandradewi, J., Prévôt, A. S., Szidat, S., Perron, N., Alfara, M. R., Lanz, V. A., Weingartner, E., and Baltensperger, U.: Using aerosol light absorption measurements for the quantitative determination of wood burning and traffic emission contributions to particulate matter, *Environ. Sci. Technol.*, 42, 3316–3323, 2008.
- Schnaiter, M., Linke, C., Möhler, O., Naumann, K. H., Saathoff, H., Wagner, R., Schurath, U., and Wehner, B.: Absorption amplification of black carbon internally mixed with secondary organic aerosol, *J. Geophys. Res.-Atmos.*, 110, D19204, <https://doi.org/10.1029/2005JD006046>, 2005.
- Schuster, G. L., Dubovik, O., and Holben, B. N.: Angstrom exponent and bimodal aerosol size distributions, *J. Geophys. Res.-Atmos.*, 111, D07207, <https://doi.org/10.1029/2005JD006328>, 2006.
- Shen, Y., Virkkula, A., Ding, A., Wang, J., Chi, X., Nie, W., Qi, X., Huang, X., Liu, Q., Zheng, L., Xu, Z., Petäjä, T., Aalto, P. P., Fu, C., and Kulmala, M.: Aerosol optical properties at SORPES in Nanjing, east China, *Atmos. Chem. Phys.*, 18, 5265–5292, <https://doi.org/10.5194/acp-18-5265-2018>, 2018.
- Sheridan, P. J. and Ogren, J. A.: Observations of the vertical and regional variability of aerosol optical properties over central and eastern North America, *J. Geophys. Res.-Atmos.*, 104, 16793–16805, 1999.
- Sherman, J. P., Sheridan, P. J., Ogren, J. A., Andrews, E., Hageman, D., Schmeisser, L., Jefferson, A., and Sharma, S.: A multi-year study of lower tropospheric aerosol variability and systematic relationships from four North American regions, *Atmos. Chem. Phys.*, 15, 12487–12517, <https://doi.org/10.5194/acp-15-12487-2015>, 2015.
- Stocker, T. F., Dahe, Q., and Plattner, G.-K.: Climate Change 2013: The Physical Science Basis, Working Group I Contribution to the

- Fifth Assessment Report of the Intergovernmental Panel on Climate Change, Summary for Policymakers (IPCC, 2013), 2013.
- Tørseth, K., Aas, W., Breivik, K., Fjæraa, A. M., Fiebig, M., Hjellbrekke, A. G., Lund Myhre, C., Solberg, S., and Yttri, K. E.: Introduction to the European Monitoring and Evaluation Programme (EMEP) and observed atmospheric composition change during 1972–2009, *Atmos. Chem. Phys.*, 12, 5447–5481, <https://doi.org/10.5194/acp-12-5447-2012>, 2012.
- Tunved, P., Hansson, H.-C., Kerminen, V.-M., Ström, J., Dal Maso, M., Lihavainen, H., Viisanen, Y., Aalto, P., Komppula, M., and Kulmala, M.: High natural aerosol loading over boreal forests, *Science*, 312, 261–263, 2006.
- Warren, S. and Wiscombe, W.: A model for the spectral albedo of snow. II: Snow containing atmospheric aerosols, *J. Atmos. Sci.*, 37, 2734–2745, 1980.
- Weatherhead, E. C., Wielicki, B. A., Ramaswamy, V., Abbott, M., Ackerman, T. P., Atlas, R., Brasseur, G., Bruhwiler, L., Busalacchi, A. J., Butler, J. H., Clack, C. T. M., Cooke, R., Cucurull, L., Davis, S. M., English, J. M., Fahey, D. W., Fine, S. S., Lazo, J. K., Liang, S., Loeb, N. G., Rignot, E., Soden, B., Stanitski, D., Stephens, G., Tapley, B. D., Thompson, A. M., Trenberth, K. E., and Wuebbles, D.: Designing the climate observing system of the future, *Earth's Future*, 6, 80–102, 2018.
- Wild, M.: Global dimming and brightening: A review, *J. Geophys. Res.-Atmos.*, 114, D00d16, <https://doi.org/10.1029/2008jd011470>, 2009.
- Wild, M.: Enlightening global dimming and brightening, *B. Am. Meteorol. Soc.*, 93, 27–37, 2012.
- Virkkula, A., Backman, J., Aalto, P. P., Hulkkoenen, M., Riuttanen, L., Nieminen, T., dal Maso, M., Sogacheva, L., de Leeuw, G., and Kulmala, M.: Seasonal cycle, size dependencies, and source analyses of aerosol optical properties at the SMEAR II measurement station in Hyytiälä, Finland, *Atmos. Chem. Phys.*, 11, 4445–4468, <https://doi.org/10.5194/acp-11-4445-2011>, 2011.
- WMO/GAW: Aerosol Measurement Procedures, Guidelines and Recommendations, GAW Report No. 153, World Meteorological Organization, Geneva, Switzerland, 2003.
- WMO/GAW: Recommendations for a Composite Surface-Based Aerosol Network, GAW Report No. 207, World Meteorological Organization, Geneva, Switzerland, 2012.
- WMO/GAW: Aerosol Measurement Procedures, Guidelines and Recommendations, 2nd edition, GAW Report No. 227, World Meteorological Organization, Geneva, Switzerland, 2016.
- Zhang, R., Khalizov, A. F., Pagels, J., Zhang, D., Xue, H., and McMurry, P. H.: Variability in morphology, hygroscopicity, and optical properties of soot aerosols during atmospheric processing, *P. Natl. Acad. Sci. USA*, 105, 10291–10296, 2008.
- Zieger, P., Aalto, P. P., Aaltonen, V., Äijälä, M., Backman, J., Hong, J., Komppula, M., Krejci, R., Laborde, M., Lampilahti, J., de Leeuw, G., Pfüller, A., Rosati, B., Tesche, M., Tunved, P., Väänänen, R., and Petäjä, T.: Low hygroscopic scattering enhancement of boreal aerosol and the implications for a columnar optical closure study, *Atmos. Chem. Phys.*, 15, 7247–7267, <https://doi.org/10.5194/acp-15-7247-2015>, 2015.
- Zotter, P., Herich, H., Gysel, M., El-Haddad, I., Zhang, Y., Močnik, G., Hüglin, C., Baltensperger, U., Szidat, S., and Prévôt, A. S. H.: Evaluation of the absorption Ångström exponents for traffic and wood burning in the Aethalometer-based source apportionment using radiocarbon measurements of ambient aerosol, *Atmos. Chem. Phys.*, 17, 4229–4249, <https://doi.org/10.5194/acp-17-4229-2017>, 2017.

Supplement of Atmos. Chem. Phys., 19, 11363–11382, 2019
<https://doi.org/10.5194/acp-19-11363-2019-supplement>
© Author(s) 2019. This work is distributed under
the Creative Commons Attribution 4.0 License.



Atmospheric
Chemistry
and Physics
Open Access
EGU

Supplement of

Over a 10-year record of aerosol optical properties at SMEAR II

Krista Luoma et al.

Correspondence to: Krista Luoma (krista.q.luoma@helsinki.fi) and Aki Virkkula (aki.virkkula@fmi.fi)

The copyright of individual parts of the supplement might differ from the CC BY 4.0 License.

S1. Data coverage

The data coverage for each month is presented in Table S1. The data coverage is presented separately for σ_{sca} and σ_{abs} . The Table S1 shows clearly how the data coverage improved from the beginning of the measurements to 2017. The data was quality assured by the author. Data was invalidated if the instrument had mechanical problems or if the RH in the instrument exceeded

5 40 %.

Table S1. Data coverage of the extensive AOPs. The data coverage is presented as percentages for each month.

Data coverage (%)	Jan	Feb	Mar	Apr	May	Jun	Jul	Aug	Sep	Oct	Nov	Dec
2006	σ_{sca}	-	-	-	-	29	54	25	28	64	99	42
	σ_{abs}	-	-	-	-	27	52	25	27	64	100	43
2007	σ_{sca}	0	54	100	99	76	81	3	9	46	51	71
	σ_{abs}	0	53	99	99	76	81	2	08	46	58	83
2008	σ_{sca}	100	99	100	93	99	45	14	10	57	68	98
	σ_{abs}	99	96	100	92	99	44	13	10	55	67	97
2009	σ_{sca}	100	100	100	100	34	0	0	15	33	83	97
	σ_{abs}	97	99	100	100	38	0	0	14	32	85	98
2010	σ_{sca}	100	97	28	0	0	76	93	92	100	15	0
	σ_{abs}	86	80	28	0	0	77	92	90	100	15	0
2011	σ_{sca}	96	98	87	79	84	90	31	85	100	84	100
	σ_{abs}	76	0	74	100	98	100	63	100	100	85	100
2012	σ_{sca}	98	99	99	100	100	97	98	100	98	100	100
	σ_{abs}	98	100	99	100	82	28	0	0	0	0	0
2013	σ_{sca}	97	51	79	100	100	100	100	100	100	100	96
	σ_{abs}	0	0	79	100	100	100	100	100	99	99	89
2014	σ_{sca}	77	92	98	100	100	100	100	100	100	100	97
	σ_{abs}	70	91	98	100	100	99	100	100	100	99	100
2015	σ_{sca}	100	100	100	100	100	100	100	100	100	99	41
	σ_{abs}	0	0	0	0	89	95	100	99	100	91	69
2016	σ_{sca}	100	100	100	100	100	100	100	84	100	100	97
	σ_{abs}	94	100	100	99	99	100	100	87	99	100	100
2017	σ_{sca}	100	100	100	92	100	100	100	98	100	100	38
	σ_{abs}	100	100	99	65	95	99	99	96	100	100	14

S2. Seasonal environmental variables for calculating the RFE

The seasonal variability of the environmental parameters (D , R_s , A_c , and RH) used in calculating the seasonal radiative effective forcing (RFE_S and $\text{RFE}_{S,\text{moist}}$) are presented in Fig. S1. The fractional daylength (D) was calculated for the latitude of 61°N and the seasonal variation of D is presented in Fig. S1a. The surface reflectance (R_s) was determined by using the surface

5 reflectance measurements by Kuusinen et al., (2012) and the seasonal variation of R_s is presented in Fig. S1b. The cloud fraction was measured (A_c) by a ceilometer that was deployed to a nearby airport that is located about 25 km from SMEAR II.

The monthly means were calculated by using data from 2010 to 2017 and the seasonal variation is presented in Fig. S1c. The relative humidity (RH) measurements were conducted with a RH sensor (Rotronic model MP102H) at 16 m height at SMEAR II. We used measurements from 2012 to 2017 in calculating the monthly means that are presented in Fig. S1d. For the D and

10 R_s we used daily values and for the A_c and RH the monthly means were used in calculating the RFE

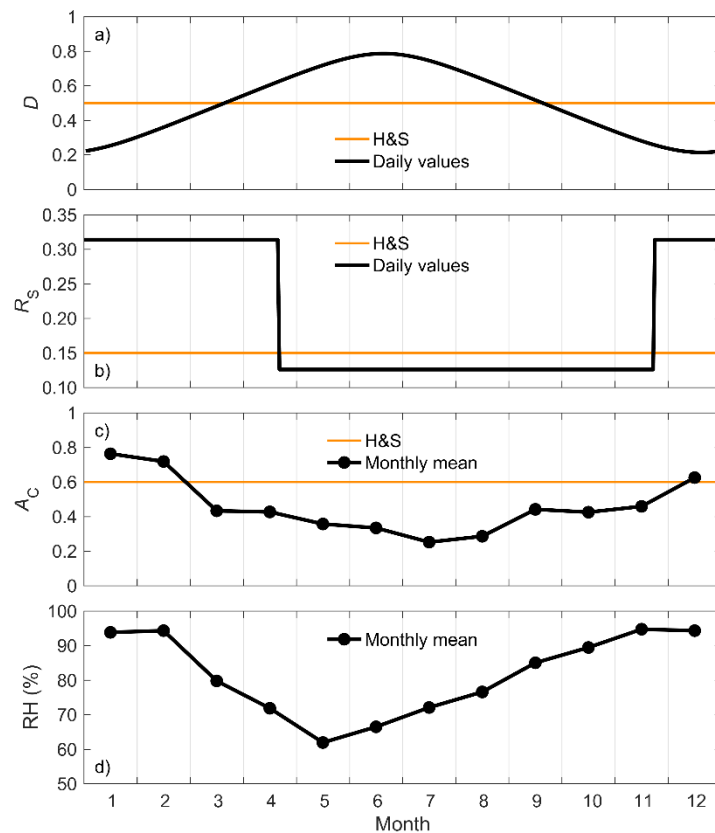


Figure S1: Seasonality of a) the fractional day length (D), b) the surface reflectance (R_s), c) the cloud fraction (A_c), and d) the relative humidity (RH). In calculating the RFEs and $\text{RFE}_{S,\text{moist}}$, we used daily values for D and R_s , and monthly means for A_c and RH. The orange line represents the constant values suggested by Haywood and Shine (1995), which were used in calculating the $\text{RFE}_{\text{H\&S}}$.

S3. Aethalometer data processing

S3.1 Flow correction

The flow reported by the Aethalometer was corrected by using the weekly flow measurements conducted at SMEAR II with a Gilian flow meter. For correcting the flow we used a three-month moving average of the measured flow. The corrected flow
5 is presented in Fig. S2.

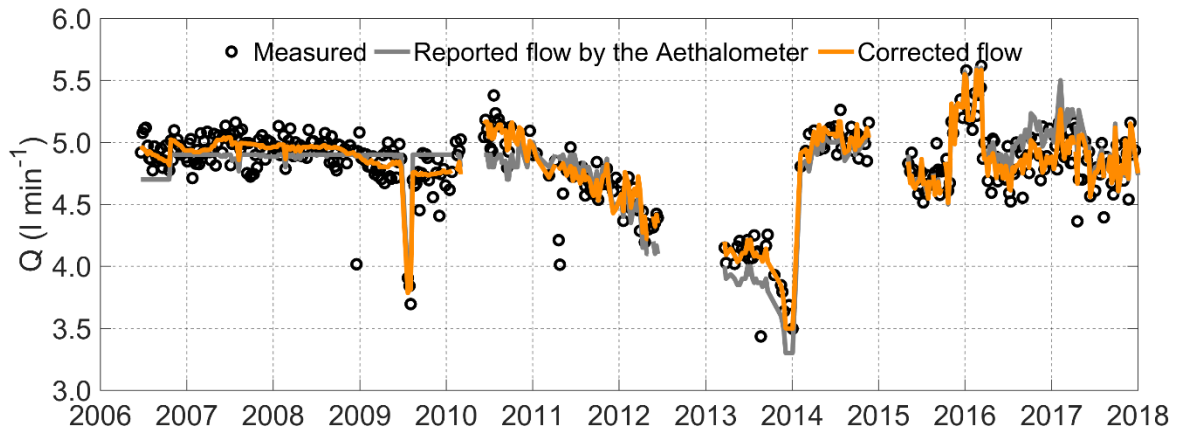


Figure S2: The Aethalometer flow (Q) correction. The black circles represent the flow measurements that were conducted almost every week at SMEAR II. The gray line is the flow that was reported by the Aethalometer and the orange line represents the corrected flow that was used in the data analysis.

S3.2 Difference between correction algorithms

In Table S2, we present values for PM10 AOPs that depend on the σ_{abs} . In Table S2, the absorption data was corrected with the correction algorithm that was suggested by Arnott et al., (2005) with a $C_{\text{ref}} = 3.688$ at $\lambda = 520$ nm in a similar manner to
10 Virkkula et al. (2011). However, the results may vary from Virkkula et al., (2011), since we used a spot size correction and a flow correction.

By comparing Table S2 to the Table 1 in the main article, we see that there is no large difference between the measured σ_{abs} at 520 nm. Since the σ_{abs} is rather similar, there is no notable difference in ω_0 either. There is a larger difference, however, in σ_{abs}
20 at other wavelengths. This causes the α_{abs} to be remarkably higher than the α_{abs} that was determined for data, which was corrected with the algorithm described in the main article. We also did the trend analysis for the data corrected with the algorithm by Arnott et al., (2005). The slope of the σ_{abs} statistically significant trend was $-0.085 \text{ Mm}^{-1}\text{yr}^{-1}$ ($-6 \% \text{yr}^{-1}$), which was similar to the trend determined with the new algorithm by Collaud Coen et al., (2010).

Table S2. PM10 AOPs derived from Aethalometer data that was corrected with the algorithm described by Arnott et al. (2005).

PM10	λ (nm)	mean \pm SD	1 %	10 %	25 %	50 %	75 %	90 %	99 %
σ_{abs} (Mm ⁻¹)	370	3.3 \pm 3.9	0.2	0.6	1.1	2.1	4.1	7.3	19.4
	520	2.1 \pm 2.4	0.1	0.4	0.7	1.4	2.6	4.7	12.0
	950	1.0 \pm 1.1	-0.1	0.1	0.3	0.6	1.2	2.2	5.3
ω_0	450	0.88 \pm 0.08	0.63	0.79	0.84	0.89	0.93	0.95	0.99
	550	0.87 \pm 0.09	0.62	0.78	0.84	0.89	0.92	0.95	0.99
	700	0.85 \pm 0.09	0.56	0.75	0.81	0.87	0.91	0.95	0.99
α_{abs}	370/520	1.30 \pm 0.60	0.16	0.85	1.10	1.30	1.46	1.68	2.86
	370/950	1.36 \pm 0.51	0.28	0.92	1.16	1.34	1.49	1.71	3.31
	470/950	1.43 \pm 0.63	0.12	0.98	1.23	1.40	1.55	1.81	3.86
RFE_{H&S} (Wm ⁻²)	550	-22 \pm 8	-33	-29	-27	-23	-19	-15	-3

S4. Uncertainty analysis

- 5 We determined the uncertainties for the intensive PM10 AOPs using the equations presented in the supplementary material by Sherman et al. (2015). The absolute and fractional uncertainties are presented in Table S3. Here we used fractional uncertainties of 9.2 %, 8.0 %, and 23 % for the PM10 σ_{sca} , σ_{psca} , and σ_{abs} , respectively. Since the uncertainties depend on the measured values, we used the mean values presented in Table 1 of the main article.
- 10 **Table S3: Uncertainties for different intensive AOPs.** Fractional uncertainty is the absolute uncertainty divided by the mean value of the AOP. The uncertainties for ω_0 , b , and RFE_{H&S} were determined at 550 nm. The uncertainty for α_{sca} was determined for the wavelength range 450–700 nm, and the uncertainty for the α_{abs} was determined for the wavelength range 370–950 nm.

	Absolute uncertainty	Fractional uncertainty (%)
$\Delta\omega_0$	0.018	2.1
Δb	0.003	2.2
$\Delta\alpha_{\text{sca}}$	0.044	2.5
$\Delta\alpha_{\text{abs}}$	0.26	27.7
$\Delta\text{RFE}_{\text{H\&S}}$ (Wm ⁻²)	1.42	6.5

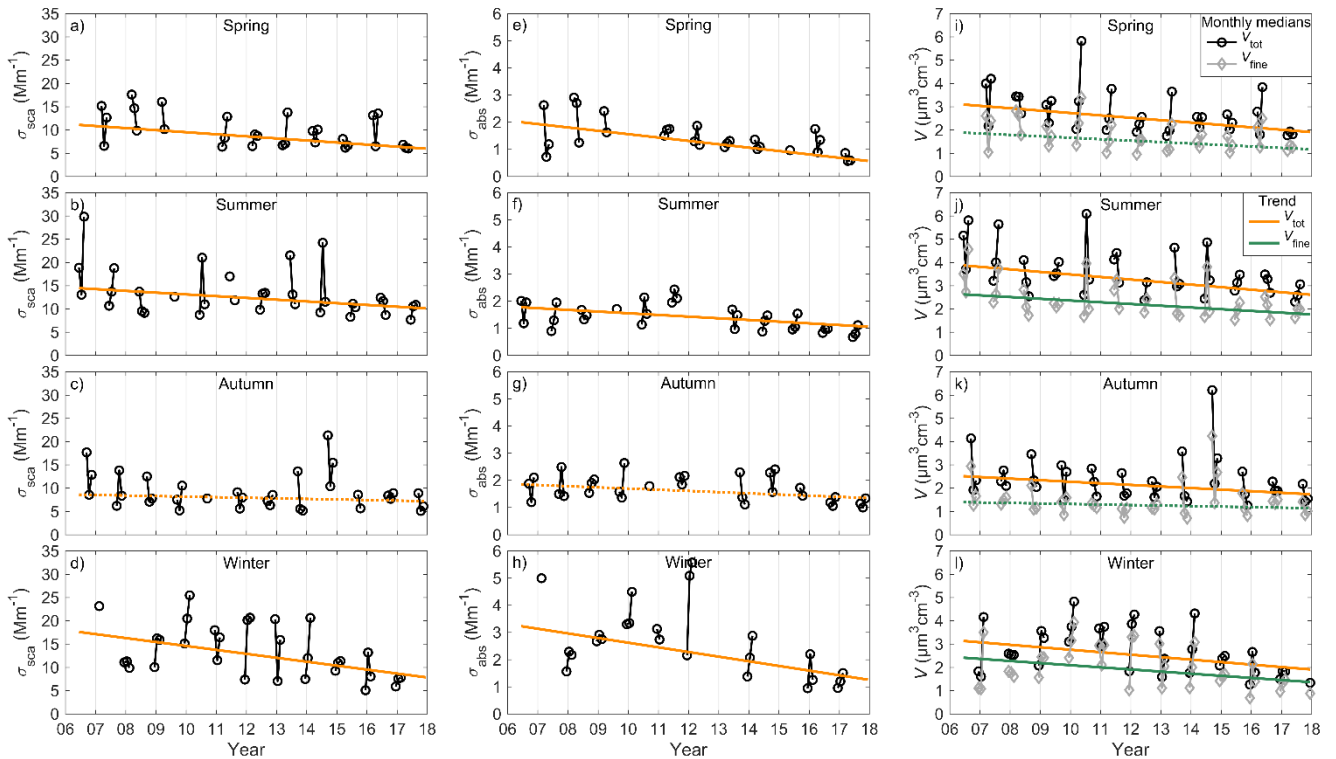
S5. Seasonality of the trends

Fig. S3 presents the time series of the σ_{sca} , σ_{abs} , V_{tot} , and V_{fine} monthly medians separately for spring, summer, autumn, and

15 winter. Fig. S3 reveals the the year-to-year variability between different seasons and it seems that in winter the variation from

the fitted trend line is the highest. This is probably due to changes in the meteorological conditions. For example, according to the statistics provided by the FMI (FMI: <http://ilmatieteenlaitos.fi/vuositilastot>, in Finnish only, last access: 25 March 2019) winter 2008 (December 2007 – February 2008) was exceptionally warm and the air masses arriving to Finland were mostly from the South and South-West that explains the low concentrations. On the contrary, high concentrations were measured in 5 winter 2010, which was according to the reports by the FMI notably colder than average. It also seems from Figs. S3c, h, and g that the concentration in winter increased from 2006 to 2010 after which it started to decrease. For other seasons we do not observe this kind of variation.

We did a similar analysis for the seasonal trends of V_{tot} and V_{fine} as we did for the σ_{sca} and σ_{abs} in the main article. The results 10 are presented in Table S3. For V_{tot} we observed a significant decreasing trend for all seasons and for V_{fine} we observed significant trends for spring, summer, and winter. For the V_{tot} the relative trends were rather similar for all the seasons; the relative trends of V_{fine} had more variation between the seasons. The variation of V_{fine} relative trends was similar to that of the σ_{sca} and σ_{abs} ; the trends were most negative in winter and spring, and least negative in summer. This analysis would suggest that the variation of the σ_{sca} and σ_{abs} seasonal trends was due to varying trends in fine particle concentration.



15

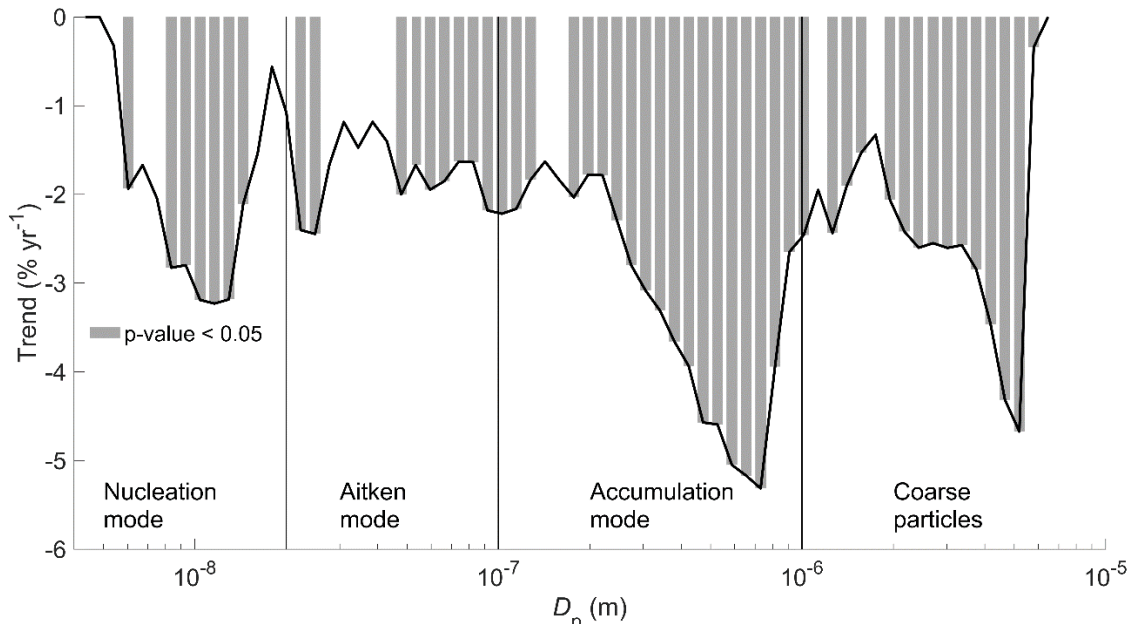
Figure S3: Monthly median values of a) – d) σ_{sca} , e) – h) σ_{abs} , and i) – l) V_{tot} (black) and V_{fine} (gray), and their trends. If the trend was statistically significant, the line is uniform and if the p value of the trend was > 0.05 , the line is dashed.

Table S4: The seasonal trend for V_{tot} and V_{fine} .

	Trend (yr ⁻¹)	Lower (yr ⁻¹)	Upper (yr ⁻¹)	p-value	Trend (yr ⁻¹)	Lower (yr ⁻¹)	Upper (yr ⁻¹)	p-value		
Spring	-0.10	-4 %	-0.20	-0.04	< 0.01	-0.06	-4 %	-0.15	0.00	0.07
Summer	-0.11	-3 %	-0.20	-0.03	< 0.01	-0.07	-3 %	-0.14	-0.02	< 0.01
Autumn	-0.07	-3 %	-0.11	-0.02	< 0.01	-0.02	-2 %	-0.07	0.01	0.23
Winter	-0.11	-4 %	-0.21	-0.01	< 0.05	-0.09	-5 %	-0.18	-0.00	< 0.05

S6. The trend of size distribution

- 5 The trend for the size distribution was determined by applying the seasonal Kendall test to each channel of the TDMPS and APS. The results are shown in Fig. S4 that presents statistically significant decreasing trends for most of the measurement channels. The relative trend was the most negative (about -5 % yr⁻¹) for particles that were about 500 – 800 nm in diameter. Fig. S6 shows that the particle volume size distribution typically has a peak around 200 – 400 nm so the largest decrease occurs on the larger side of the accumulation mode.



10 **Figure S4: Trend analysis for the size distribution. The solid line represents the average trend in percentages. The gray bars mark the size ranges, in which the trend was statistically significant (p -value < 0.05). The typical borders of the nucleation, Aitken, accumulation and coarse particle modes are marked with vertical lines.**

S7. The seasonal variation of the size distribution

Fig. S5 presents the seasonal variation of the geometrical mean diameter (GMD), the volume mean diameter for fine particles ($D_p < 1 \mu\text{m}$, VMD_{fine}) and the volume mean diameter for all particles ($D_p < 10 \mu\text{m}$, VMD_{tot}). The seasonal variation of the size distribution helps interpreting the seasonal variation of the σ_{sca} PM1/PM10 ratio, α_{sca} and b that are sensitive to different size ranges.

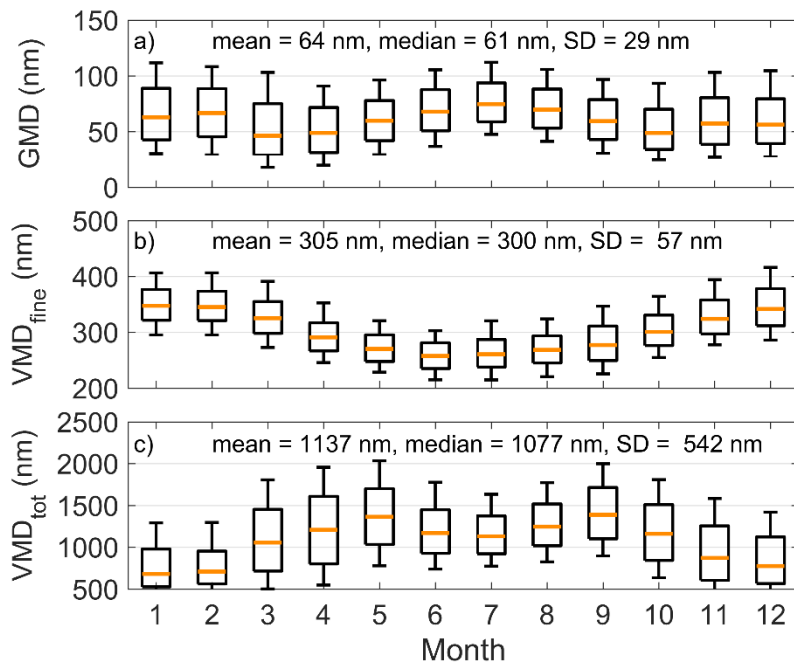


Figure S5: The seasonal variation and statistics for a) the GMD, b) the VMD_{fine}, and c) VMD_{tot}.

S8. Effect of excluding the moist data on the seasonal variation

Fig. S6 presents the monthly median values of different AOP for the dry data only and for a data set that included the moist data as well. The moist nephelometer data was corrected to dry conditions by using the equations and parameters presented in Sect. 2.3.1. Since the moist data occurred in summer and autumn, the difference between the different data sets is the highest from June to October.

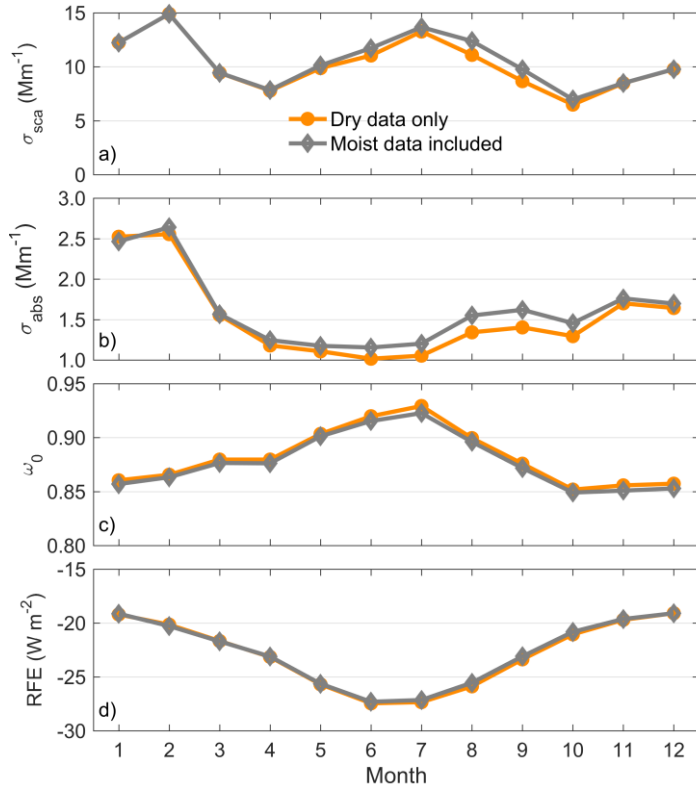


Figure S6: Monthly median values of a) σ_{sca} , b) σ_{abs} , c) ω , and d) RFE. The orange line presents the median values for the data set from where the moist periods before 2010 were excluded and the gray line represents a data set where all the data were taken into account.